

Response functions as diagnostics of the broad-line region in active galactic nuclei

M. R. Goad,¹ P. T. O'Brien¹ and P. M. Gondhalekar²

¹*Department of Physics & Astronomy, University College London, Gower Street, London WC1E 6BT*

²*Rutherford Appleton Laboratory, Chilton, Didcot, Oxon OX11 0QX*

Accepted 1993 January 15. Received 1992 December 7; in original form 1992 June 17

ABSTRACT

We present response functions for a large number of emission lines covering a wide variety of ionization states emitted from a spherical broad-line region (BLR). The line emissivities are calculated using a photoionization code for a cloud distribution where the cloud properties and covering factor are constrained by a pressure law. Emissivity-weighted and responsivity-weighted response functions are compared for different lines emitted from the same spatially extended BLR gas, and we discuss their dependences on the radial ionization parameter and density gradients. Depending on the local physical conditions, we show that some lines can have negative response functions, particularly if the BLR contains a region of optically thin clouds. This possibility has important implications for attempts to deduce the BLR structure from monitoring data, and is inconsistent with the assumption, implicit in the maximum entropy method, that the response function is positive.

We find that comparison of the response functions for lines of different ionization states is a powerful diagnostic of the run of physical conditions in the BLR. In particular, we show that the observed difference in the lag of the high- and low-ionization lines can be reproduced even when these lines are emitted by the same ensemble of clouds, and therefore that different geometries for the clouds that emit these lines may not be required. We discuss the suitability of various lines for the determination of the structure of the BLR, and how the blend mean wavelength of several strong blended lines varies following a continuum event. The models are also compared with monitoring data for several active galactic nuclei.

Key words: radiative transfer – techniques: spectroscopic – galaxies: active – galaxies: nuclei – quasars: emission lines.

1 INTRODUCTION

Models of the broad-line region (BLR) in active galactic nuclei (AGN) use measurements of the intensities of a large number of emission lines covering a range of ionization states to determine the physical properties of the BLR gas, and to constrain the spectral characteristics of the ionizing continuum. Comparison of the observed line ratios with photoionization calculations has led to the development of a model in which the BLR consists of a large number of small, high-density, high column density clouds of roughly solar chemical composition. These clouds are optically thick to the Lyman continuum, and are photoionized by a luminous central source of UV and X-ray radiation (Davidson & Netzer 1979; Kwan & Krolik 1981). This so-called ‘standard

model’ of the BLR is characterized by single values for the ionization parameter U and hydrogen density N , which are related by the expression

$$U = \frac{Q(h)}{4\pi r^2 N c}, \quad (1)$$

where $Q(h)$ is the number of hydrogen ionizing photons per second, r is the distance of the cloud from the ionizing continuum source, and c is the velocity of light. Typically, $U \sim 10^{-2}$ and $N \sim 10^{9.5} \text{ cm}^{-3}$ reproduce the observed line ratios of a large number of lines to within a factor of a few.

Despite its apparent success, the standard model does have some major problems. One of the most important is the failure of the model to reproduce, simultaneously, the

intensities of both the high-ionization lines (HILs: e.g. O ν λ 1035, N ν λ 1240 and He Π λ 1640) and the low-ionization lines (LILs: e.g. H β , Mg Π λ 2798 and Fe Π lines) – the ‘energy budget’ problem (Netzer 1985; Collin-Souffrin 1986). This observational constraint, coupled with differences in line profiles and redshifts (Gaskell 1982; Wilkes 1984), has led several authors to propose BLRs which incorporate gas with a wide range of physical parameters, including the possibility of several components with distinct geometries and kinematics. In particular, the presence of high column density gas has been invoked, primarily to enhance the emission of the LILs through additional heating by X-ray and infrared radiation. This gas may be in the form of an accretion disc (Collin-Souffrin 1987; Dumont & Collin-Souffrin 1990), with most of the HIL emission arising from surrounding lower density, lower column density clouds. Ferland & Persson (1989) also proposed high column density gas, which may be in the form of a wind from a star or accretion disc. However, their model produces both the HILs and LILs from the same gas by invoking a high ionization parameter ($U > 10^{-1}$), which is consistent with recent variability data (see below).

To discriminate between the proposed BLR models, we need to utilize as many observational constraints as possible. Apart from the comparison of line ratios, profiles and redshifts, an additional and potentially very powerful constraint comes from the monitoring of continuum and emission-line variability – the ‘reverberation mapping’ technique – where the continuum and emission-line variations are related by the ‘response function’ (Blandford & McKee 1982). In practice, due to the generally poor sampling of light curves, most variability analyses to date have concentrated on obtaining the cross-correlation function (CCF) rather than attempting to recover the response function. The peak (or lag), centroid and overall shape of the CCF can place some constraints on the BLR if a geometry is assumed (Gaskell & Sparke 1986; Gaskell & Peterson 1987; Robinson & Pérez 1990). Rearrangement of equation (1) implies a BLR radius $r = 63 [Q(h)/10^{54}]^{0.5} (U/0.01)^{-0.5} (N/10^{10})^{-0.5}$ light-day. Thus the standard model predicts $r \sim 10^2$ light-day for Seyfert 1 galaxies and $r \sim 10^3$ light-day for QSOs. The observed lag derived from the CCF peak is typically about an order of magnitude smaller (Peterson 1988, and references therein). This discrepancy may arise from incorrect assumptions when interpreting the variability data (Penston 1991), but taken at face value the small lags imply smaller BLR radii and hence higher photon densities than in the standard model. If the mean density estimates are reasonable, as seems likely given the observed intercombination line intensities, then the mean ionization parameter must be higher than previously thought. The lag is observed to differ amongst different lines in the same AGN, although there is no clear pattern in this behaviour amongst different AGN. In NGC 5548 the lag is larger and the variability amplitude smaller for the LILs compared to the HILs (Clavel et al. 1991). In contrast, in NGC 4151 the C iv λ 1549 and Mg Π λ 2798 lines have a similar variability time-scale and amplitude, whereas the C iii] λ 1909 line varies more slowly and weakly (Clavel et al. 1990; Ulrich et al. 1991).

Clearly, if we are to make progress in the utilization of variability data to constrain the BLR structure and the

physical properties of the gas, it is necessary to predict the detailed response of different lines to variations in the ionizing continuum. That aim is the main purpose of this paper, in which we compare the responses of a large number of lines of different ionization states within the context of a well-defined BLR model. The observational data show that realistic BLR models must encompass clouds with a broad range of density, ionization parameter and column density. Assumptions about which lines dominate at particular radii, by arbitrary parametrization of the radial line emissivity distribution, are likely to be inaccurate. We adopt the approach of Rees, Netzer & Ferland (1989, hereafter RNF), and use a photoionization code to calculate the emission-line spectrum of a family of spherical BLR models in which both the physical properties and the spatial distribution of the clouds are constrained by a pressure law which is a power law in radius. This approach, although not unique, has the advantage that the radial dependences of a large number of physical parameters are constrained in a self-consistent manner. In this paper we consider only spherical BLR models. It is unclear at present whether the results from the most intensive monitoring campaigns require a non-spherical BLR or different components producing the LILs and HILs (Maoz et al. 1991; Krolik et al. 1991; Horne, Welsh & Peterson 1991; Ferland et al. 1992). To draw such conclusions requires comparison of the observations with the kind of detailed physical models presented here.

To provide a basic set of models relative to which variations occur, we describe in Section 2 a set of ‘steady-state’ spherical BLRs defined by different pressure laws. These models are normalized to represent a typical low-luminosity AGN. For each model the emissivities for individual clouds are calculated, and then integrated over the BLR to determine the line and continuum luminosities. In Section 3 we discuss the reverberation mapping technique, and present two sets of response functions, making different assumptions for each set as to how the gas responds to changes in the continuum level. For both sets of response functions we assume that, relative to the steady-state models, the lines respond linearly to changes in the continuum level and that the clouds emit isotropically. For the first set we further assume that, when the continuum level changes, the emissivity of a given line changes by the same factor for all the clouds. Hence these are effectively *emissivity-weighted* response functions. For the second set we change the continuum level by a known amount, and calculate the resultant change in line emissivities and hence the *responsivity* of the gas. These are then used to calculate *responsivity-weighted* response functions. The form of both sets of response functions and their dependences on the pressure-law index are discussed in Section 4. The usefulness of the comparative variability of certain lines as diagnostics of the BLR properties is also discussed, and the model predictions are compared with monitoring data for several AGN. Our conclusions and suggestions for future work are given in Section 5.

2 PRESSURE-LAW BLR MODELS

The multi-cloud BLR models described in this and subsequent papers were produced using the computer code PROSYN (Goad & O'Brien 1991; Goad, in preparation).

PROSYN can model BLRs with a wide range of geometrical configurations and velocity laws. Clouds are placed randomly within a six-dimensional phase space permitted by the particular model, and assigned a line emissivity. The emissivities are either relative (using an assumed functional form) or, as here, calculated using a photoionization code. PROSYN then calculates the line luminosities, profiles and response functions. The model response functions can be compared with recovered response functions, or they can be convolved with continuum light curves to produce model-line light curves, trailed spectrograms and time-averaged line profiles for direct comparison with monitoring data.

As in RNF and Netzer (1991), we model a spherical BLR, with inner and outer radii R_{in} and R_{out} respectively. The model BLR is populated with spherical clouds in pressure balance with the intercloud medium. For the pressure P we take

$$P(r) \propto r^{-s}. \quad (2)$$

Making the reasonable assumption that the gas kinetic temperature is a weak function of U , we then assume that the density is given by

$$N(r) \propto r^{-s}. \quad (3)$$

This gives a radial dependence for the ionization parameter:

$$U(r) \propto r^{s-2}. \quad (4)$$

For constant-density spherical clouds with radius R_c , whose individual masses are conserved as they move in or out as part of some flow, $R_c^3 N = \text{constant}$. Thus the cloud cross-sectional area A_c can be expressed as

$$A_c(r) \propto R_c^2 \propto r^{2s/3}, \quad (5)$$

and the column density N_{col} as

$$N_{\text{col}}(r) \propto R_c N \propto r^{-2s/3}. \quad (6)$$

We also assume that the cloud velocity v is a power-law function with radius,

$$v(r) \propto r^{-t}, \quad (7)$$

and that the cloud number density is given by

$$n_c(r) \propto r^{-p}. \quad (8)$$

If the clouds move with their virial velocity ($t=1/2$), then imposition of mass conservation ($n_c v r^2 = \text{constant}$) requires $p=2-t$, which gives the radial dependence of the differential covering factor dC as

$$dC(r) \propto A_c(r) n_c(r) dr \propto r^{(2s/3)-(3/2)} dr \propto r^\gamma dr. \quad (9)$$

Hence a complete pressure-law BLR model can be specified by providing values for the pressure-law index s , R_{in} and R_{out} , and by normalizing U , N , N_{col} and dC at some radius.

2.1 Steady-state models

Having decided on the functional form for the variation of the cloud parameters with radius, we calculated what will henceforth be referred to as a set of five ‘steady-state’ pressure-law BLR models. By ‘steady-state’ we mean that the continuum flux and line emissivities have remained constant for a time greater than the light-crossing time of the BLR [$= 2 \times (R_{\text{out}}/c)$]. Any change in the continuum flux at future times will cause changes in the line emissivities relative to these steady-state models.

The line and continuum radial emissivity distributions $\varepsilon(r)$ were calculated using the photoionization code CLOUDY (version 80.06: Ferland 1991; Ferland et al. 1992) for five different values of s : 2.0, 1.5, 1.0, 0.5 and 0.0. The parameters describing the models are given in Table 1. To aid comparison with RNF, the models are labelled B to F following their notation (hence no model A). The input ionizing

Table 1. Steady-state model parameters.

Parameter	Model B	Model C	Model D	Model E	Model F
s	2	$\frac{3}{2}$	1	$\frac{1}{2}$	0
γ	$-\frac{1}{6}$	$-\frac{3}{6}$	$-\frac{5}{6}$	$-\frac{7}{6}$	$-\frac{9}{6}$
$\log r(N = 10^{10} \text{ cm}^{-3}) \text{ cm}$	16.413	16.413	16.413	16.413	16.413
$\log U(N = 10^{10} \text{ cm}^{-3})$	-2.000	-2.000	-2.000	-2.000	-2.000
$\log N_{\text{col}}(N = 10^{10} \text{ cm}^{-3}) \text{ cm}^{-2}$	22.000	22.000	22.666	22.833	23.750
$\log R_{\text{in}} \text{ cm}$	14.913	14.913	14.913	14.913	14.913
$\log R_{\text{out}} \text{ cm}$	17.163	17.163	17.163	17.163	17.163
$\log U(R_{\text{in}})$	-2.000	-1.250	-0.500	0.250	1.000
$\log U(R_{\text{out}})$	-2.000	-2.375	-2.750	-3.125	-3.500
$\log N(R_{\text{in}}) \text{ cm}^{-3}$	13.000	12.250	11.500	10.750	10.000
$\log N(R_{\text{out}}) \text{ cm}^{-3}$	8.500	8.875	9.250	9.625	10.000
$\log N_{\text{col}}(R_{\text{in}}) \text{ cm}^{-2}$	24.000	23.500	23.666	23.333	23.750
$\log N_{\text{col}}(R_{\text{out}}) \text{ cm}^{-2}$	21.000	21.250	22.167	22.583	23.750

continuum was CLOUDY's table AGN option, which is similar to that described by Mathews & Ferland (1987), and is fairly typical for radio-quiet AGN. The submillimetre break was set at 10 μm , and at longer wavelengths the continuum has a slope of $f_\nu \propto \nu^{5/2}$. Strong far-infrared radiation is seen from many AGN, but much of this radiation, particularly in radio-quiet objects, may be due to thermal emission from dust covering a very large radius range (Sanders et al. 1989). As seen by a BLR cloud, this radiation would therefore be weak relative to the ionizing UV and X-ray continua from the central source. Setting of the submillimetre break at longer wavelengths has the effect of increasing the importance of free-free heating, which particularly enhances high-ionization lines such as C IV $\lambda 1549$ and O VI $\lambda 1035$ (Ferland & Persson 1989; Ferland et al. 1992).

As one aim of this paper is to explore how the choice of the pressure-law index s affects the form of the response functions for different lines, all the models shown here have the same physical dimensions. We adopted the physical dimensions of RNF's model B, which, allowing for the lower source luminosity used here, gives values for R_{in} and R_{out} of 0.316 and 56.23 light-day respectively. The reason for setting the outer radius as described in RNF remains valid for all the models shown here (i.e. $[\text{O III}] \lambda 4363/\text{H}\beta \leq 0.1$). The inner radius was set to avoid densities $> 10^{13} \text{ cm}^{-3}$, as CLOUDY's numerical methods are unreliable at higher densities. Such clouds are weak line emitters in any case. The specific abundances used were 'solar' as given by Grevesse & Anders (1989) (He: C: N: O: Ne: Mg: Al: Si: S: Ar: Ca: Fe)/H = $(10^4: 36.3: 11.2: 85.1: 12.3: 3.8: 0.295: 3.55: 1.62: 0.363: 0.229: 4.68) \times 10^{-5}$. Individual clouds were assumed to have a constant density, although constant-pressure clouds gave very similar results.

The ionization parameter and density were normalized to $U = 10^{-2}$ and $N = 10^{10} \text{ cm}^{-3}$ at a radius of 10 light-day, typical of the observed lag for Seyfert 1 galaxies. The normalization corresponds to a total luminosity in the ionizing continuum, L_{ion} , of $10^{42.22} \text{ erg s}^{-1}$ [$Q(h) = 10^{52.4} \text{ photon s}^{-1}$ – approximately half of the luminosity of NGC 4151]. The models can be adjusted to a different luminosity by appropriate scaling of the radii ($r \propto L_{\text{ion}}^{0.5}$). The column density was normalized to make most clouds optically thick at the Lyman limit, although models B, E and F contain some optically thin clouds (Section 3.1.2). The covering factor was normalized such that the source was totally covered at the outer radius. Hence, for comparison with actual AGN, the calculated line luminosities should be multiplied by more realistic covering factors, which are typically thought to lie in the range 0.1–0.5 (Smith et al. 1981). The values of γ (equation 9) for each model are given in Table 1, and Fig. 1 shows the cumulative covering factor for each model as a function of radius. As s decreases, γ becomes more negative, thereby placing a higher fraction of the gas at smaller radii.

The total number of clouds was arbitrarily set at 500 000 (the finite number sets a limit on the resolution). The clouds were assumed to move in an r^{-1} gravitational potential, following randomly inclined circular Keplerian orbits. The velocity at the inner radius was set at 10^4 km s^{-1} , which is a typical half-width at zero intensity (HWZI) for the broad emission lines in AGN. This corresponds to a central black hole mass of $10^{6.8} M_\odot$, and a Schwarzschild radius

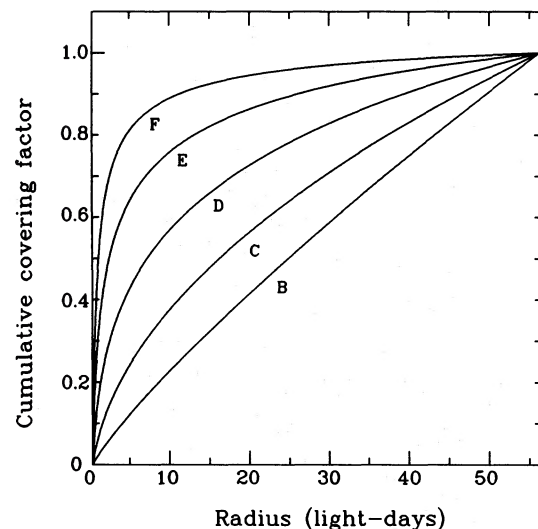


Figure 1. Variation of the cumulative covering factor with radius.

$R_s = 0.0007$ light-day. Accretion disc models (e.g. Krolik et al. 1991) suggest that, if the UV and X-ray continua arise from such discs, R_{in} is large enough ($450 R_s$) for a point-source ionizing continuum to be a reasonable approximation. The Eddington limit for this source is $L_{\text{Edd}} = 10^{44.90} \text{ erg s}^{-1}$, which gives $L_{\text{ion}}/L_{\text{Edd}} = 0.002$.

2.1.1 Line and continuum emissivities

The logarithms of the steady-state model radial emissivity distributions (for 17 emission lines and the Balmer and Paschen continua) divided by the local density, $\log[\epsilon(r)/N(r)]$, are shown in Fig. 2 for model B. A subset of these data is shown in Fig. 3 for models C–F. The emissivities were calculated at a large number of radii, and intermediate values were obtained by linear interpolation in log space. In these models the density varies as a power law with radius. Hence, if the radial emissivity distributions were also well described by power laws, the $\log[\epsilon(r)/N(r)]$ distributions in Figs 2 and 3 would be straight lines. This is a poor approximation to $\epsilon(r)$ for many lines, particularly where there is a large radial density gradient or a mixture of optically thick and thin gas. As the physics of BLR gas similar to that used in our models has been discussed extensively elsewhere (RNF; Ferland & Persson 1989; Ferland et al. 1992), we will discuss only the form of the variations in $\epsilon(r)$ with density, ionization parameter and column density required for interpretation of differences in the response functions. The general form of the normalized emissivity distributions shown in Figs 2 and 3 is similar to those presented by RNF, although there are some differences resulting from our use of an updated version of CLOUDY and different abundances, and the enforcement of identical R_{in} and R_{out} for all the models.

For models E and F, the clouds in the inner BLR ($r < 6$ light-day) are unstable with respect to disruption by radiation pressure, mainly due to Ly α . Models E and F are more susceptible to this problem than are models B, C and D, as they have lower densities when the ionization parameter is large. Such clouds would not be stable if supported by an external medium alone (Elitzur & Ferland 1986). Other

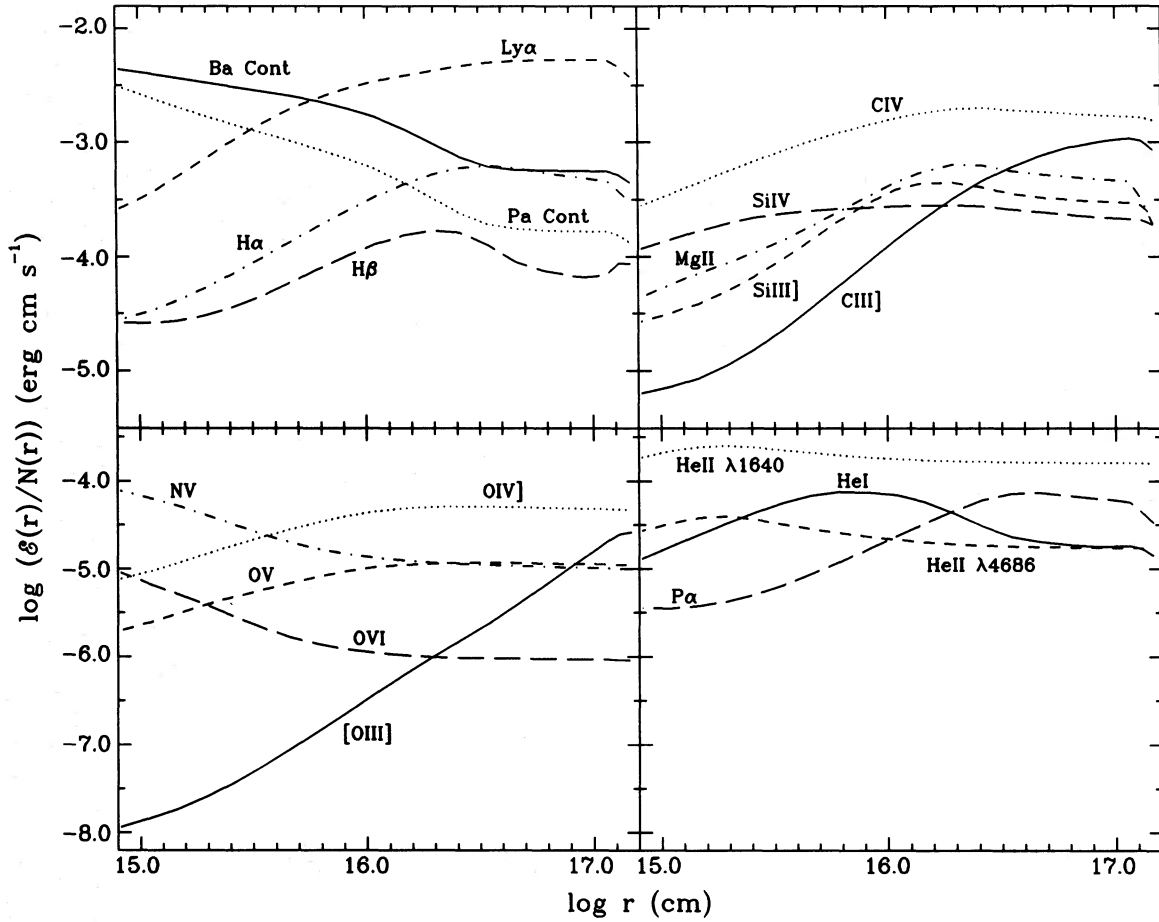


Figure 2. The line and continuum emissivities divided by the local density $[\epsilon(r)/N(r)]$ for steady-state model B. Lines or continua for which $\epsilon(r)$ is well approximated by a power law with radius would show up as straight lines. This is a poor approximation for many lines.

mechanisms, however, such as magnetic fields (Rees 1987), may provide support. None of the models considered here has a substantial optical depth to electron scattering.

2.1.2 Integrated emission-line spectra

The total luminosities (L_{tot}) of each line and continuum for the steady-state models were found by integrating over radius between $r = R_1$ and $r = R_2$ ($R_1 \leq R_2$), using

$$L_{\text{tot}} \propto 4\pi \int_{R_1}^{R_2} \epsilon(r) A_c(r) n_c(r) r^2 dr. \quad (10)$$

The line and continuum ratios with respect to $H\beta$, along with $L_{\text{tot}}(H\beta)$ (erg s^{-1}), are given in the first columns of Table 2 for each model, integrated from R_{in} to R_{out} . To investigate the effect of a smaller range in radius, we also give in the second columns of Table 2 the results of integrating from R_{in} to the half-radius, HR , which we define as $(R_{\text{in}} + R_{\text{out}})/2$ ($= 28.275$ light-day). This differs from the approach used by RNF, who defined the half-radius as the point at which $L_{\text{tot}}(H\beta)$ falls to exactly half its value at R_{out} . We use HR , as we wish to compare models with identical physical dimensions. Comparing the first column of Table 2 for model B (i.e. integrating to R_{out}) with the results of RNF, we find no significant differences in the line ratios, and the values of $L_{\text{tot}}(H\beta)$ agree to within 6 per cent, taking into account the different con-

tinuum luminosities. There are some differences in the line ratios for model B, due to the changes in the photoionization code and chemical abundances used here. The line ratios for models C and D cannot be compared directly to RNF, as we use different values of R_{in} and R_{out} , and hence have different ranges in U , N and N_{co} .

3 REVERBERATION MAPPING

The analyses of BLR spectra show that the cloud densities are sufficiently high for recombination time-scales to be very short (\sim minutes). The clouds are also small enough for the ionization fronts to adjust their positions on short time-scales (\sim hours). Hence the response of the BLR is assumed to be dominated by light-traveltime effects. The following assumptions are also made here: (i) the ionizing continuum originates from a point source; (ii) the ionizing continuum is emitted isotropically; (iii) the ionizing continuum shape remains constant when the continuum level changes; (iv) obscuration effects due to shadowing or dust are negligible; (v) relativistic effects are ignored; (vi) line photons are not scattered by an intercloud medium; (vii) all lines are emitted isotropically; and (viii) all lines respond linearly to changes in the ionizing continuum. These assumptions may be relaxed, in a model-dependent way, and these issues will be discussed in subsequent papers.

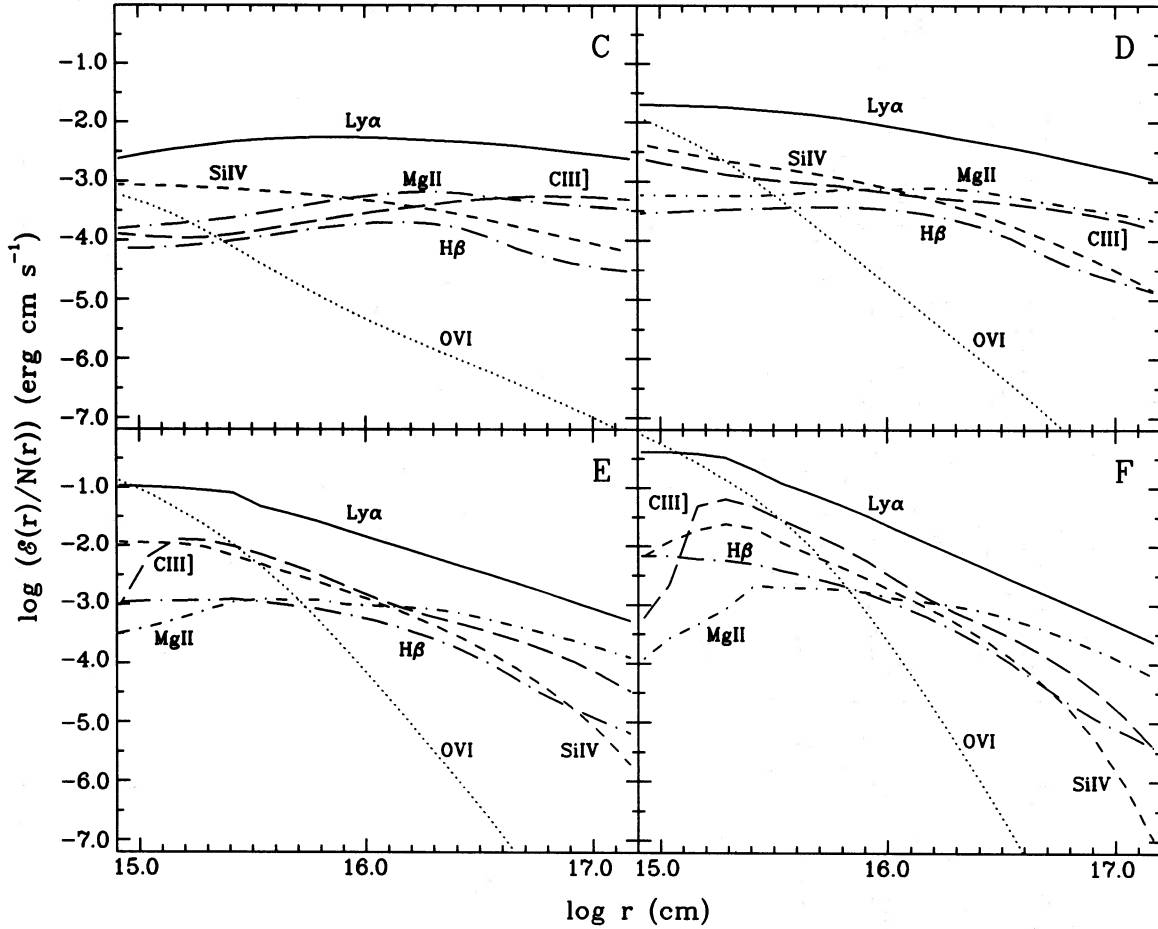


Figure 3. As Fig. 2, for steady-state models C, D, E and F (only a subset of the data is shown).

The reverberation mapping technique involves measuring the delay between the time at which an observer sees variations in the continuum flux, which is viewed directly, and the time at which they see variations in the line flux from the spatially extended BLR, which occur later due to the longer photon flight path (Blandford & McKee 1982). Consider a BLR cloud at position (r, θ) , where r is the distance of the cloud from the continuum source, and θ is the angle between the cloud radius vector and the line of sight to the distant observer, measured from the side nearest to the observer. As seen by the observer, the cloud will respond to a continuum 'event' after a time-delay $\tau = (r/c)(1 - \cos \theta)$. Thus clouds observed to respond to the continuum event after a time-delay τ lie on a paraboloidal surface of constant delay τ . The primary aim of reverberation mapping is to recover the BLR response function, $\Psi(v, \tau)$, which relates the emission-line and continuum light curves $L(v, t)$ and $C(t)$ as functions of τ , time t and velocity v through the expression

$$L(v, t) = \int_0^\infty \Psi(v, \tau) C(t - \tau) d\tau. \quad (11)$$

By comparison with models, the form of the one-dimensional $\Psi(\tau)$ derived from integrated line fluxes can constrain the BLR geometry far better than can the CCF, but recovery of $\Psi(v, \tau)$ from line profile variations is preferred, as then both

the BLR geometry and the kinematics can be deduced. In this paper, we only consider the form of $\Psi(\tau)$ for a spherical geometry. The form of $\Psi(v, \tau)$ for several other geometries and various velocity laws is discussed elsewhere (e.g. Walsh & Horne 1991; Goad & O'Brien 1991; Mannucci, Salvati & Stanga 1992; Pérez, Robinson & de la Fuente 1992b; O'Brien, Goad & Gondhalekar 1993a, in preparation).

As well as deducing the geometry and kinematics of the BLR, comparison of the response functions for different lines combined with photoionization calculations can be used to derive the physical conditions in the BLR. To do this reliably, however, we need to consider the detailed relationship between the line emissivity and the continuum level. This relationship does not alter the boundaries of $\Psi(v, \tau)$ in the v - τ plane, which depend *only* on the geometry and kinematics, but it does strongly affect the amplitude of $\Psi(v, \tau)$ within those boundaries, possibly rendering parts of the v - τ plane observationally undetectable. If the relationship is not taken into account, therefore, incorrect conclusions about the BLR properties may be drawn from response functions recovered from monitoring data (Section 4.3). Large line optical depths can also alter the amplitude of the response function, by preventing line photons emitted from parts of the BLR phase space from reaching the observer (Ferland et al. 1992; Goad & O'Brien 1993; O'Brien et al. 1993a, in preparation).

Table 2. Integrated intensities relative to H β and the total luminosity of H β (erg s $^{-1}$) for the steady-state models. For each model, the two columns correspond to termination of the integration at the outer radius (R_{out}) and at the half-radius (HR), respectively.

	Model B		Model C		Model D		Model E		Model F	
	R_{out}	HR	R_{out}	HR	R_{out}	HR	R_{out}	HR	R_{out}	HR
Ba Cont	9.09	10.0	11.1	12.1	13.0	14.3	12.0	12.7	12.4	12.7
Pa Cont	3.26	3.85	4.16	4.74	5.46	6.16	4.38	4.68	5.45	5.64
O VI $\lambda 1035$	0.01	0.01	0.06	0.07	0.44	0.52	2.39	2.67	5.83	6.13
Ly α $\lambda 1215$	49.1	39.6	47.1	37.4	38.4	32.7	36.8	33.7	28.7	27.3
O V $\lambda 1218$	0.12	0.10	0.13	0.15	0.40	0.47	1.15	1.28	1.97	2.07
N V $\lambda 1240$	0.13	0.12	0.21	0.26	0.48	0.57	0.84	0.94	0.77	0.81
Si IV $\lambda 1397$	2.52	2.32	2.36	2.36	2.08	2.24	2.28	2.47	1.82	1.90
O IV] $\lambda 1402$	0.51	0.42	0.47	0.47	0.54	0.61	0.80	0.88	0.95	1.00
C IV $\lambda 1549$	18.2	15.7	14.9	15.0	13.4	14.9	15.6	17.1	14.5	15.2
He II $\lambda 1640$	1.80	1.58	1.81	1.68	1.77	1.77	2.13	2.20	2.39	2.45
Si III] $\lambda 1893$	3.32	3.03	3.57	3.04	3.05	2.73	2.54	2.39	1.62	1.57
C III] $\lambda 1909$	7.83	4.79	6.53	3.97	4.33	3.27	3.89	3.73	3.93	4.03
Mg II $\lambda 2798$	4.84	4.55	5.88	4.50	5.51	4.07	4.54	3.35	2.82	2.16
[O III] $\lambda 4363$	0.10	0.03	0.04	0.02	0.02	0.01	0.02	0.02	0.04	0.04
He II $\lambda 4686$	0.20	0.18	0.21	0.20	0.22	0.22	0.27	0.28	0.32	0.33
H β $\lambda 4861$	1.00	1.00	1.00	1.00	1.00	1.00	1.00	1.00	1.00	1.00
He I $\lambda 5876$	0.29	0.32	0.33	0.35	0.35	0.37	0.35	0.36	0.31	0.32
H α $\lambda 6563$	5.00	4.48	4.90	4.15	4.21	3.69	3.69	3.29	2.93	2.66
Pa α $\lambda 18751$	0.57	0.49	0.54	0.43	0.44	0.36	0.35	0.30	0.27	0.23
$\log L_{\text{tot}}(\text{H}\beta)$	39.89	39.71	39.90	39.79	39.94	39.86	39.87	39.83	39.85	39.83

In using the response function as defined in equation (11), we are implicitly assuming that the line emissivity is linearly proportional to the continuum level. This is a poor approximation when considering a wide range in continuum level. However, the relationship is reasonably linear when considering a small range in continuum level about some mean level, assuming that the clouds remain optically thick. Thus we can redefine the response function in equation (11) to relate *changes* in line emissivity to *changes* in the continuum level. The response function is then measuring the partial derivative of the line emissivity with respect to changes in the continuum level about the mean level – the *responsivity* of the gas – integrated over the surface of constant time-delay (Krolik et al. 1991; Sparke 1993). If we further assume that the cloud density does not vary significantly when the continuum level changes, the required partial derivative is then that of the line emissivity with respect to changes in U . Following Krolik et al., we quantify the line responsivity for the linear response approximation using a radial variable $\eta(r)$, such that

$$\frac{\delta \varepsilon(r)}{\bar{\varepsilon}(r)} = \eta(r) \frac{\delta U(r)}{\bar{U}(r)}, \quad (12)$$

where $\bar{\varepsilon}(r)$ and $\bar{U}(r)$ are the local mean line emissivity and ionization parameter. Here we calculate two sets of response

functions, making different assumptions for $\eta(r)$, and taking $\bar{\varepsilon}(r)$ and $\bar{U}(r)$ from the steady-state models.

3.1 Response functions

3.1.1 Emissivity-weighting

For the first set of response functions we assume that, when the continuum level changes, the emissivity of a given line changes by the same factor for all the clouds (i.e. η is constant for a given line throughout the BLR). Assumption of a constant η means that the form of $\varepsilon(r)$ is maintained when the continuum level changes, and hence the corresponding $\Psi(\tau)$ is effectively *emissivity-weighted*. The emissivity-weighted $\Psi(\tau)$ is either entirely positive ($\eta > 0$) or entirely negative ($\eta < 0$). If we also assume isotropically emitting clouds, then the response function for a thin spherical shell of gas of radius R_{sh} which responds in this way is flat from $\tau=0$ until $\tau=2(R_{\text{sh}}/c)$, and zero at all other times. The response function for a geometrically thick sphere can then be thought of as the sum of a set of response functions for a series of thin spherical shells of radius $R_{\text{in}} \leq R_{\text{sh}} \leq R_{\text{out}}$. The resultant $\Psi(\tau)$ is flat from $\tau=0$ until $\tau=2(R_{\text{in}}/c)$, and then goes to zero at $\tau=2(R_{\text{out}}/c)$. The rate at which $\Psi(\tau)$ goes to zero for $\tau > 2(R_{\text{in}}/c)$ depends on how rapidly the line emission varies as a function of radius.

Table 3. The centroids of the emissivity-weighted response functions – the emissivity-weighted radii (R_{EW}) (light-day). The values of η used to calculate these response functions are given in the second column.

	η	Model					
		B	C	D	E	F	
Ba Cont	1.0	17.8	12.1	7.2	5.7	3.7	
Pa Cont	1.0	15.3	10.0	5.9	5.5	3.8	
O VI $\lambda 1035$	4.5	22.3	2.0	0.8	0.7	0.8	
Ly α $\lambda 1215$	0.9	27.5	24.3	19.5	13.6	8.7	
O V $\lambda 1218$	3.4	26.6	9.9	2.3	1.3	1.1	
N V $\lambda 1240$	3.2	22.1	6.2	2.1	1.5	1.6	
Si IV $\lambda 1397$	1.6	24.3	17.3	10.7	6.0	4.1	
O IV $\lambda 1402$	2.0	26.5	16.8	7.4	3.4	1.9	
C IV $\lambda 1549$	2.0	26.0	17.5	9.6	5.3	3.5	
He II $\lambda 1640$	1.0	24.8	19.0	12.6	7.1	3.5	
Si III $\lambda 1893$	0.8	24.9	22.5	18.3	13.9	10.0	
C III $\lambda 1909$	1.0	32.3	30.0	23.2	11.9	5.0	
Mg II $\lambda 2798$	0.5	24.5	25.4	24.1	22.4	20.0	
[O III] $\lambda 4363$	1.2	40.1	35.7	24.7	8.6	2.3	
He II $\lambda 4686$	1.0	23.9	17.8	11.4	6.3	3.1	
H β $\lambda 4861$	1.1	23.0	18.1	14.6	11.0	7.5	
He I $\lambda 5876$	1.0	18.6	14.3	10.2	7.6	5.5	
H α $\lambda 6563$	1.0	25.8	23.4	19.9	16.5	12.6	
P α $\lambda 18751$	1.0	27.0	25.4	22.1	18.9	15.6	

To calculate the emissivity-weighted $\Psi(\tau)$, clouds were chosen randomly in θ about the central source at 0.01-light-day intervals in radius from R_{in} to R_{out} . The contributions of individual clouds were then calculated from the steady-state model emissivities, the η s and the cloud cross-sectional areas, and summed in 0.3-d time-delay bins from $\tau=0$ to $2(R_{out}/c)$. The values of η used for each line are given in the second column of Table 3, and range from 0.5 to 4.5, indicating the wide range in response of different lines to the same change in continuum level. The values of η given in Table 3 actually correspond to those at a radius of 25 light-day in model D calculated in Section 3.1.2, and should only be considered as illustrative. For most lines, $\eta(r)$ varies significantly with radius. The resultant emissivity-weighted $\Psi(\tau)$ s for all the models are shown in Fig. 4, excluding the weak [O III] $\lambda 4363$ line and the continua. Each $\Psi(\tau)$ was normalized to unity at the peak for convenience in plotting. The small value of R_{in} (0.316 light-day) makes it difficult to see the flat part of the emissivity-weighted $\Psi(\tau)$ s on the scale of Fig. 4.

To provide a ‘characteristic’ BLR size for each line, the centroid of the emissivity-weighted $\Psi(\tau)$ – the *emissivity-weighted radius* (R_{EW}) – is given in Table 3. The variation of R_{EW} with s is shown in Fig. 5(a). The observed trends in R_{EW} with s are similar if the $\Psi(\tau)$ s are computed by integrating to HR rather than to R_{out} , although obviously the centroids are then smaller. The form of the emissivity-weighted $\Psi(\tau)$, and hence the value of R_{EW} , is independent of η for a given line,

whereas its absolute amplitude, and hence the line response amplitude, depends linearly on η .

3.1.2 Responsivity-weighting

For the second set of response functions we ‘perturbed’ the steady-state models by changing the continuum level (and hence U) and determined a new set of emissivity values. The radial $\eta(r)$ distributions were then calculated from the change in emissivity between the perturbed and steady-state models relative to the change in U using equation (12). We increased the ionization parameter by 0.1 in the log relative to the steady-state model, equivalent to an increase in the continuum level of about 26 per cent, which is fairly typical of observed continuum variability amplitudes. The $\Psi(\tau)$ s were then derived as before, using $\eta(r)$ to weight the contribution made by each cloud. These *responsivity-weighted* $\Psi(\tau)$ s are shown in Fig. 6, again excluding the weak [O III] $\lambda 4363$ line and the continua. Each $\Psi(\tau)$ was again normalized to unity at the peak for convenience in plotting. The centroid of the responsivity-weighted $\Psi(\tau)$ for each line – the *responsivity-weighted radius* (R_{RW}) – is given in Table 4, and is shown as a function of s in Fig. 5(b).

The radial change in emissivity as a function of continuum level can be quite complex, depending on the local density, column density and ionization parameter. This is illustrated in Fig. 7, which shows the $\eta(r)$ distributions for four representative lines of models B, D and F. Models C and E are not shown, as they behave in a similar way to models D and F respectively. In general, the emissivities increase when the continuum level increases [$\eta(r) > 0$]. This is true for all lines of models C and D, in which the clouds are optically thick at the Lyman limit at all radii. For model B the clouds in the outer BLR ($r \gtrsim 43$ light-day) are optically thin at the Lyman limit due to the low column density. For models E and F the clouds in the inner BLR ($r \lesssim 1$ light-day) are also optically thin, due to the very high ionization parameter. In these optically thin regions, the hydrogen line emissivities tend to remain constant when the continuum level increases [$\eta(r) \approx 0$], whilst some LIL emissivities decrease [$\eta(r) < 0$]. Formally, this behaviour invalidates the use of a linear response approximation, but we will continue to discuss these effects in this context as they illustrate the importance of taking the detailed gas physics into account when calculating response functions and interpreting monitoring data.

If, as we are assuming here, the relationship between the emissivity and continuum level is linear, then the centroid of $\Psi(\tau)$ is equal to the *luminosity-weighted radius*, which we define as

$$R_{LW} = \frac{\int_{R_{in}}^{R_{out}} \eta(r) r L(r) dr}{\int_{R_{in}}^{R_{out}} \eta(r) L(r) dr}, \quad (13)$$

where $L(r)$ is the luminosity at radius r

$$[L(r) \propto \epsilon(r) A_c(r) n_c(r) r^2].$$

It should be noted that this definition of the luminosity-weighted radius differs from that given in the literature (e.g. Robinson & Pérez 1990), in that we allow for the radial

responsivity distribution. If η is constant, $R_{\text{LW}} = R_{\text{EW}}$, otherwise $R_{\text{LW}} = R_{\text{RW}}$. The response function centroid is also equal to the centroid of the CCF (Penston 1991; Koratkar & Gaskell 1991). The centroid can therefore be derived from the CCF without having to recover the response function. In practice, however, the accuracy with which the centroid can be recovered from either will depend strongly on the sampling rate, the data quality and the length of the sampling window (Pérez, Robinson & de la Fuente 1992a). The peak (or lag) of the CCF cannot be simply related to $\Psi(\tau)$, and can be strongly biased towards the inner radius of the BLR (Gaskell & Sparke 1986; Robinson & Pérez 1990).

Before comparing the emissivity-weighted and responsivity-weighted $\Psi(\tau)$ s in detail in Section 4, let us consider the response of two idealized BLRs, hereafter referred to as cases I and II, containing a mixture of clouds which are either optically thick or thin at the Lyman limit. We note that,

although here we discuss the case of the hydrogen ionization edge, similar arguments could be developed for other ionization edges. Cases I and II each comprise two radial regions, one containing only optically thick clouds and the other only optically thin clouds. In the spirit of the linear response approximation, we assume that the boundary radius, R_{th} , between the two regions, at which the clouds become optically thin at the Lyman limit, is independent of U over a small range in U .

For case I, the BLR clouds are assumed to be optically thin in the outer BLR for radii $R_{\text{th}} \leq r \leq R_{\text{out}}$, and $\eta(r) = 0$ for the hydrogen lines in this region. The clouds are assumed to be optically thick and $\eta(r) > 0$ for the hydrogen lines at all other radii. The responsivity-weighted $\Psi(\tau)$ for hydrogen will therefore be flat and positive for $0 \leq \tau \leq 2(R_{\text{in}}/c)$, and will then go to zero at $\tau = 2(R_{\text{th}}/c)$. Such a $\Psi(\tau)$ and associated $\eta(r)$ distribution are illustrated in Fig. 8(a). Thus for the

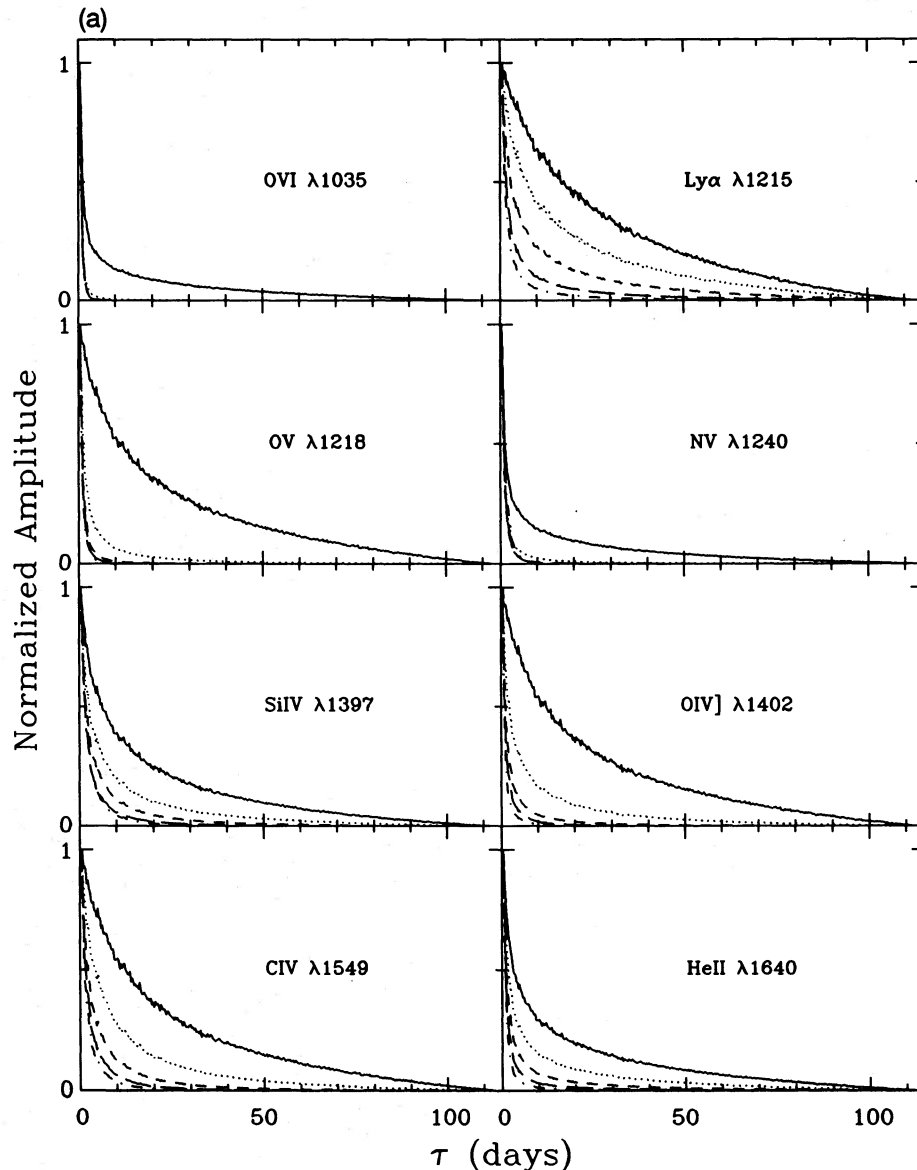


Figure 4. Emissivity-weighted response functions for all the models, for all the lines except [O III] $\lambda 4363$. The small flat section of the response functions ($\tau \leq 0.632$ light-day) is present, although difficult to discern on this scale. The response functions extend to 112.46 light-day [$\tau = 2(R_{\text{out}}/c)$]. Solid line: model B; dotted line: model C; short-dashed line: model D; long-dashed line: model E; dot-dashed line: model F.

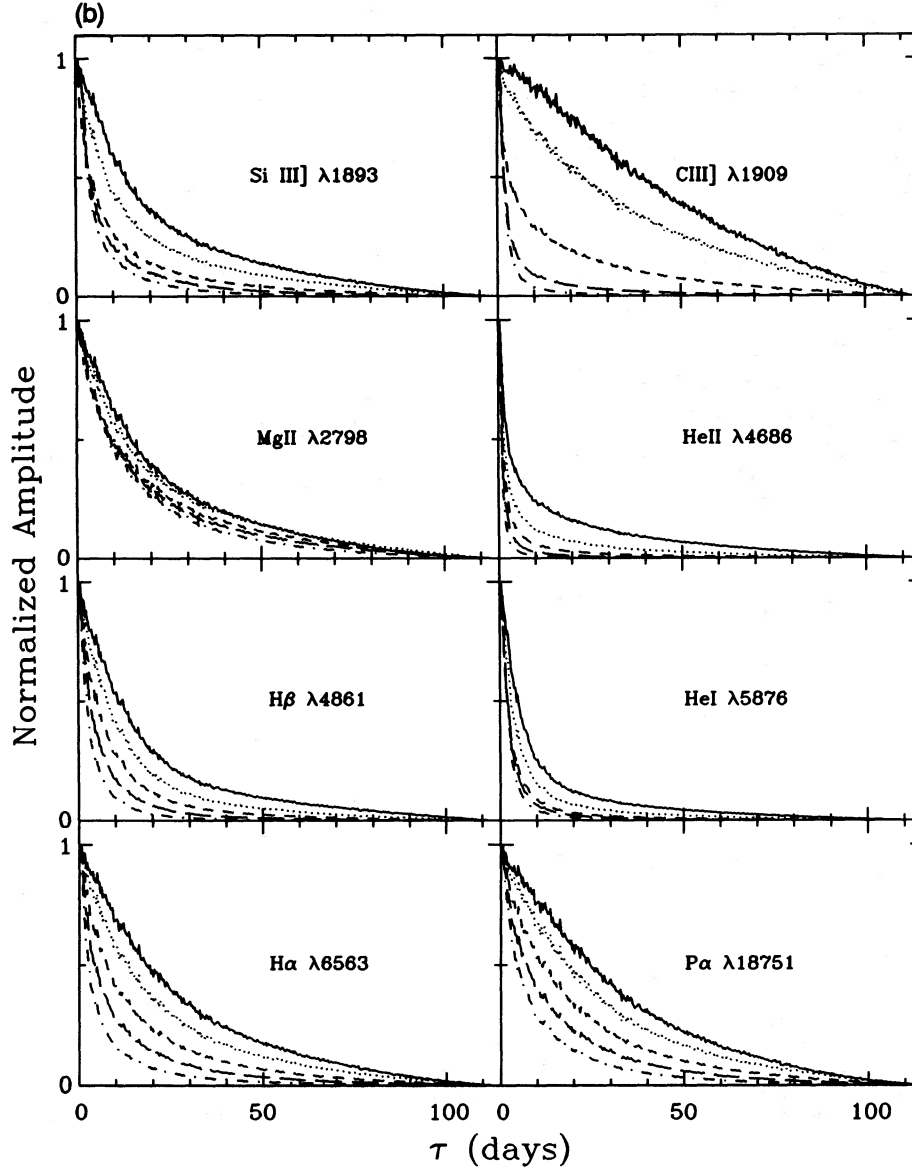


Figure 4 - continued

hydrogen lines an outer optically thin region decreases the effective outer radius of the variable BLR from R_{out} to R_{th} .

The existence of the partially ionized zone, from which the LILs mainly arise, depends on the BLR cloud having a large optical depth at the Lyman limit between the back of the cloud and the ionizing continuum source (Kwan & Krolik 1981). If the optical depth is small, an increase in the ionization parameter will tend to deplete low-ionization species from the cloud. Hence for case I the LILs will tend to have $\eta(r) < 0$ in the outer BLR for radii $R_0 < r \leq R_{\text{out}}$, where R_0 is the boundary radius at which $\eta(r) = 0$, and $\eta(r) > 0$ at smaller radii. As the abundances of the LIL species depend on the optical depth at the Lyman limit, $R_0 \approx R_{\text{th}}$. The responsivity-weighted $\Psi(\tau)$ for an LIL will therefore be flat and positive for $0 \leq \tau \leq 2(R_{\text{in}}/c)$, and will then go to zero at the time-delay for which the gas with negative responsivity has an equal relative weight to the gas with positive

responsivity on the corresponding constant-time-delay surface. This $\Psi(\tau)$ then goes negative, is most negative at $\tau = 2(R_0/c)$, and then goes to zero at $\tau = 2(R_{\text{out}}/c)$. This is illustrated in Fig. 8(b). Thus a BLR with an outer optically thin region tends to give a responsivity-weighted $\Psi(\tau)$ for an LIL which is positive at small time-delays and negative at large time-delays.

For case II the BLR clouds are assumed to be optically thin in the inner BLR for radii $R_{\text{in}} \leq r \leq R_{\text{th}}$, and $\eta(r) = 0$ for the hydrogen lines in this region. The clouds are assumed to be optically thick and $\eta(r) > 0$ for the hydrogen lines at all other radii. The responsivity-weighted $\Psi(\tau)$ for hydrogen will therefore be flat and positive for $0 \leq \tau \leq 2(R_{\text{th}}/c)$, and will then go to zero at $\tau = 2(R_{\text{out}}/c)$. This is illustrated in Fig. 8(c). Thus for the hydrogen lines an inner optically thin region increases the effective inner radius of the variable BLR from R_{in} to R_{th} .

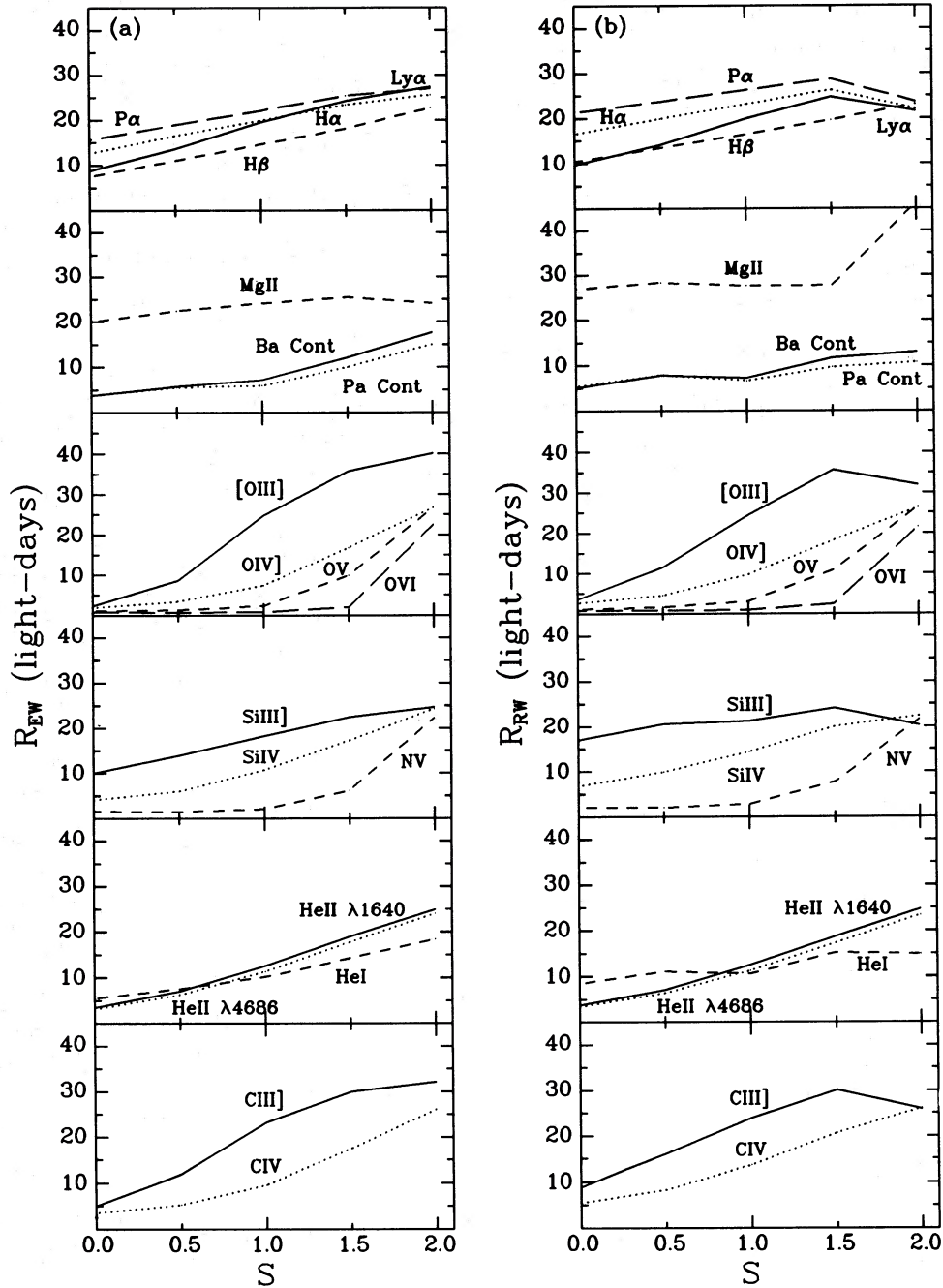


Figure 5. (a) Variation of the emissivity-weighted radius R_{EW} with the pressure-law index s . (b) Variation of the responsivity-weighted radius R_{RW} with the pressure-law index s .

In an analogous way to case I, the LILs for case II will tend to have $\eta(r) < 0$ in the inner BLR for radii $R_{in} \leq r \leq R_0$, and $\eta(r) > 0$ at larger radii. The responsivity-weighted $\Psi(\tau)$ for an LIL will therefore be flat for $0 \leq \tau \leq 2(R_{in}/c)$, will peak with positive amplitude at $\tau = 2(R_0/c)$, and will then go to zero at $\tau = 2(R_{out}/c)$. This $\Psi(\tau)$ will remain positive for $0 \leq \tau < 2(R_0/c)$, unless the gas with negative responsivity has a greater relative weight than the gas with positive responsivity on the corresponding constant-time-delay surface. An example $\Psi(\tau)$ which goes negative is illustrated in Fig. 8(d). Thus a BLR with an inner optically thin region tends to give a responsivity-weighted $\Psi(\tau)$ for an LIL which has a positive

amplitude peak at $\tau = 2(R_0/c)$, and possibly goes negative at smaller time-delays.

For a spherical BLR, including cases I and II, the responsivity-weighted $\Psi(\tau)$ for a line for which $\eta(r) > 0$ at all radii is flat and positive for $0 \leq \tau \leq 2(R_{in}/c)$ and then goes to zero at $\tau = 2(R_{out}/c)$.

4 DISCUSSION

Both the emissivity-weighted and responsivity-weighted $\Psi(\tau)$ s depend on the radial variations of $\epsilon(r)$, $A_c(r)$ and

$n_c(r)$. The responsivity-weighted $\Psi(\tau)$ s, however, also depend on $\eta(r)$. Thus, although the form of the responsivity-weighted $\Psi(\tau)$ s shown in Fig. 6 is similar to that of the emissivity-weighted $\Psi(\tau)$ s shown in Fig. 4, there are detailed differences because of the radial dependence of the responsivity.

4.1 Emissivity-weighted $\Psi(\tau)$

As the same covering-factor law is applied to every line within a given model, and η is assumed constant for a given line, the form of $\varepsilon(r)$ determines the relative contribution of each radial shell to the emissivity-weighted $\Psi(\tau)$ s. It is clear from Figs 2 and 3 that $\varepsilon(r)$ can be a complicated function of radial distance, as the strength of a particular line depends on several interrelated factors. Taking model B as an example, C III $\lambda 1909$ is collisionally de-excited when the density rises

above $\sim 10^{9.5} \text{ cm}^{-3}$, and hence contributes little emission in the inner BLR (Fig. 2). Thus this line has a large R_{EW} (the largest in model B apart from [O III] $\lambda 4363$). The fall in the emissivities of several lines, including Ly α , C IV $\lambda 1549$ and He I $\lambda 5876$, for $r \lesssim 10^{16.25} \text{ cm}$ is also due to thermalization. The importance of thermalization also depends on the optical depths, which are lower for C IV $\lambda 1549$ and He II $\lambda 4686$ than for Ly α , increasing the relative strength of the former lines at small radii. When the optically thick lines are thermalized, the cooling, and hence the emission, is increasingly dominated by HILs like O VI $\lambda 1035$, and in the densest clouds by continua. However, the very dense clouds in models B, C and D make a fairly small contribution to the total flux, due to the low covering factor at small radii (Fig. 1). We note that the O V $\lambda 1218$ line discussed by Ferland et al. (1992) is fairly weak in these models (< 7 per cent of Ly α).

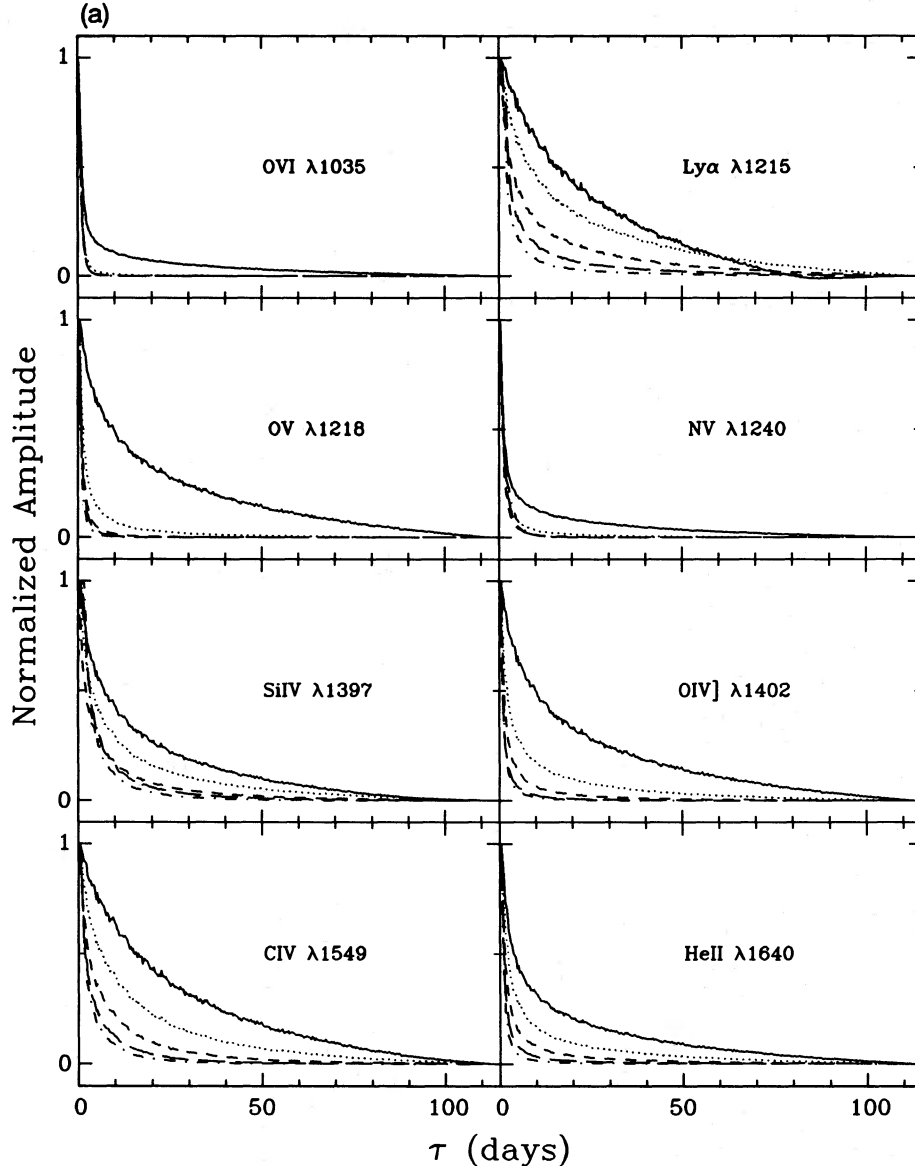


Figure 6. Responsivity-weighted response functions for all the models, for all the lines except [O III] $\lambda 4363$. Solid line: model B; dotted line: model C; short-dashed line: model D; long-dashed line: model E; dot-dashed line: model F.

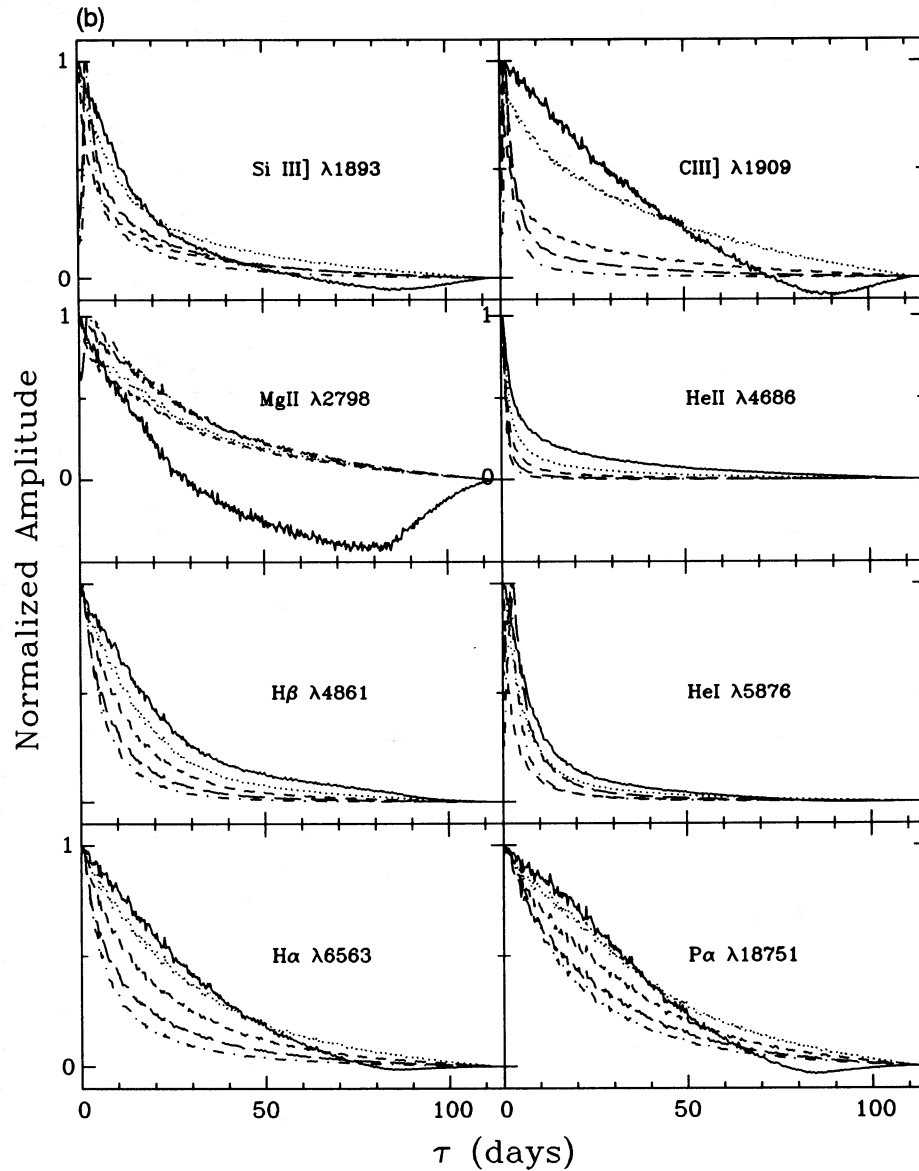


Figure 6 – continued

In going from model B to model F (decreasing s), the degree of ionization of the innermost gas increases, whilst that of the outermost gas decreases, increasing the degree of BLR stratification. Combined with the greater covering factor at small radii for smaller s (Fig. 1), this has the overall effect of increasing the ratio of HILs to LILs in the integrated spectrum. This can be seen clearly in Table 2, where HILs like $O\text{VI } \lambda 1035$ and $N\text{V } \lambda 1240$ are much stronger in the small- s models. The overall spectrum for any of the models, whether integrating to R_{out} or to HR , is fairly similar to the average AGN spectrum tabulated by Netzer (1991). Some of the usual discrepancies remain, however, including $N\text{V } \lambda 1240$ which is too weak and $\text{Ly}\alpha$ which is too strong compared to $\text{H}\beta$.

The emissivity-weighted $\Psi(\tau)$ s and R_{EW} s shown in Figs 4(a,b) and 5(a) display a variation amongst line species

within a given model which is due to the differences in $\epsilon(r)$. The characteristic BLR size therefore depends on which line is considered. For model B (constant ionization parameter), the R_{EW} s mostly cluster in a small range around 22–28 d. The exceptions are $\text{HeI } \lambda 5876$, which has an unusual emissivity curve, the $\text{CIII } \lambda 1909$ and $[\text{OIII}] \lambda 4363$ lines, which arise mainly from the outer lowest density gas, and the continua, which arise mainly from the inner high-density gas. As the value of s is decreased, the HILs become more strongly weighted towards the inner radii, and hence have smaller R_{EW} s and emissivity-weighted $\Psi(\tau)$ s which go to zero rapidly for $\tau > 2(R_{\text{in}}/c)$. The HIL R_{EW} s can be up to a factor of 30 smaller than for the LILs in the most highly stratified models. The reduction in R_{EW} with decreasing s is quite abrupt in some cases (e.g. $O\text{VI } \lambda 1035$), but is usually a fairly smooth trend (e.g. $\text{Ly}\alpha$).

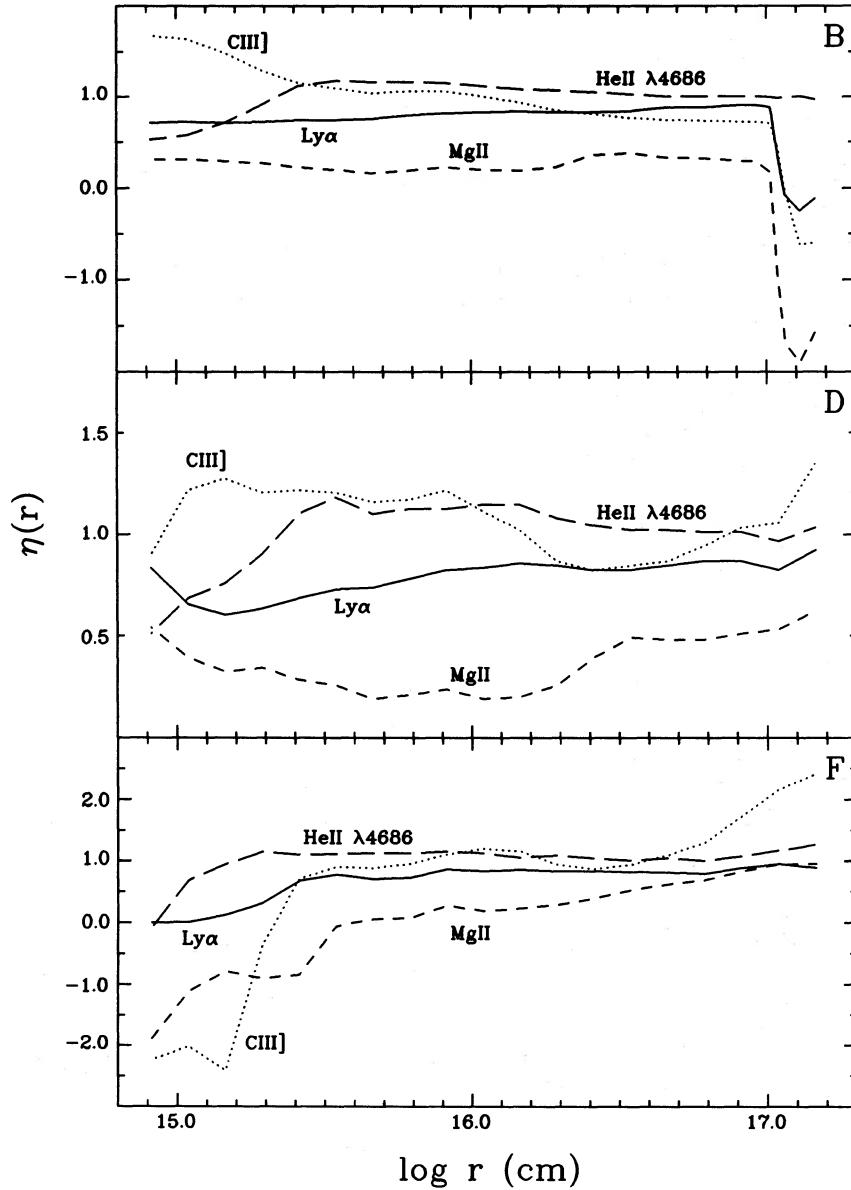


Figure 7. The Ly α (solid line), He II $\lambda 4686$ (long-dashed line), Mg II $\lambda 2798$ (short-dashed line) and C III] $\lambda 1909$ (dotted line) $\eta(r)$ distributions for models B, D and F.

4.2 Responsivity-weighted $\Psi(\tau)$

In model B the clouds are optically thin at the Lyman limit for radii larger than $R_{\text{th}} \approx 43$ light-day. This approximates the situation in the idealized case I discussed in Section 3.1.2. Unlike case I, however, the calculated $\eta(r)$ s for the Ly α , H α and Pa lines for model B are slightly negative in the outer BLR. These negative $\eta(r)$ s, combined with the large covering factor at large radii in model B, result in slightly negative responsivity-weighted $\Psi(\tau)$ s for $\tau \geq 80$ d (Fig. 6). For these lines, $R_0 \approx 43$ light-day, and hence the minima in their $\Psi(\tau)$ s occur at $\tau \approx 86$ d. The small responsivity at large radii results in $R_{\text{RW}} < R_{\text{EW}}$ for Ly α , H α and Pa in model B. For H β , the responsivity-weighted $\Psi(\tau)$ is positive at all time-delays as

$\eta(r) > 0$ at all radii, and $R_{\text{RW}} \approx R_{\text{EW}}$. Several of the LILs formed in the partially ionized zone have $\eta(r) < 0$ in the outer BLR in model B (Fig. 7), and hence have a negative responsivity-weighted $\Psi(\tau)$ at large time-delay. For C III] $\lambda 1909$, Si III] $\lambda 1893$ and Mg II $\lambda 2798$, $R_0 \approx 41$ –44 light-day, and hence the minima in their $\Psi(\tau)$ s occur at $\tau \approx 82$ –88 d. For [O III] $\lambda 4363$, which is not shown in Fig. 6, and He I $\lambda 5876$, the minimum occurs at $\tau \approx 95$ –100 d. For all these lines, $R_{\text{RW}} < R_{\text{EW}}$, except in the case of Mg II $\lambda 2798$. For this line the clouds with negative responsivity dominate for $\tau \geq 30$ d, resulting in a large negative-amplitude $\Psi(\tau)$ at large time-delay and $R_{\text{RW}} > R_{\text{EW}}$. This line is more affected than the other LILs, as $\eta(r)$ for Mg II is smaller in the inner BLR and more negative in the outer BLR where the covering factor is

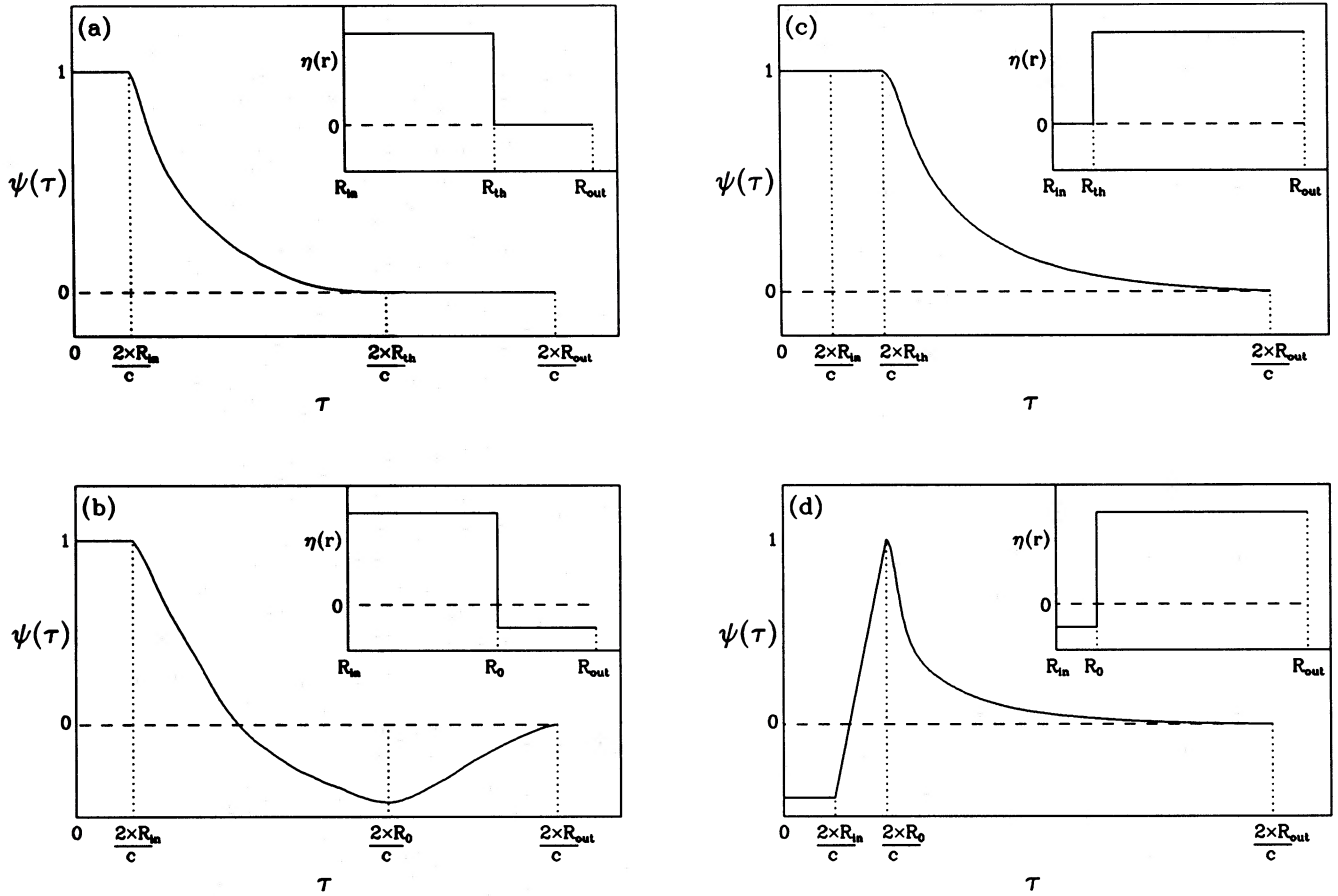


Figure 8. Example responsivity-weighted $\Psi(\tau)$ s for the idealized cases I and II. Corresponding $\eta(r)$ distributions are shown as inserts. See text for details. (a) Hydrogen lines for case I: $\Psi(\tau)$ goes to zero at $\tau = 2(R_{th}/c)$. (b) LILs for case I: the negative minimum of $\Psi(\tau)$ occurs at $\tau = 2(R_0/c)$. (c) Hydrogen lines for case II: $\Psi(\tau)$ is flat for $0 \leq \tau \leq 2(R_{th}/c)$. (d) LILs for case II: $\Psi(\tau)$ peaks at $\tau = 2(R_0/c)$, and decreases at smaller time-delay, going negative in this example, with a flat section for $0 \leq \tau \leq 2(R_{in}/c)$.

large. For the HILs, $R_{RW} \lesssim R_{EW}$ because of the general decline in $\eta(r)$ with increasing radius for these lines in model B.

The idealized case II discussed in Section 3.1.2 is similar to models E and F, in which the clouds are optically thin at the Lyman limit within a radius $R_{th} \approx 1$ light-day. For the hydrogen lines, $\eta(r) \approx 0$ in this region, resulting in $R_{RW} > R_{EW}$. The magnitude of the effect also depends on the form of $\eta(r)$ at larger radii. As $\eta(r)$ is smaller at small radii and increases faster at larger radii for $H\beta$, $H\alpha$ and $P\alpha$ compared to $Ly\alpha$, these lines show a larger increase in R_{RW} compared to R_{EW} . Several of the LILs formed in the partially ionized zone have $\eta(r) < 0$ in the innermost BLR in models E and F (Fig. 7). For the $Si\ III\ \lambda 1893$, $C\ III\ \lambda 1909$, $Mg\ II\ \lambda 2798$, $[O\ III]\ \lambda 4363$ and $He\ I\ \lambda 5876$ lines, $R_0 \approx 0.5$ – 1.5 light-day, and hence their responsivity-weighted $\Psi(\tau)$ s are flat for $0 \leq \tau \leq 0.632$ d, and then increase to peak at $\tau \approx 1$ – 3 d. All of these $\Psi(\tau)$ s remain positive, although the $C\ III\ \lambda 1909$ $\Psi(\tau)$ in model F almost goes negative at very small time-delays. This line has the most negative $\eta(r)$ in models E and F. The decrease in amplitude of the LIL responsivity-weighted $\Psi(\tau)$ s at small time-delays is greater for model F than for model E, as model F has a larger covering factor at small radii (Fig. 1). For the LILs in models

E and F, $R_{RW} > R_{EW}$, mainly because of the negative responsivity at small radii. For the HILs, $R_{RW} > R_{EW}$ because of the general increase in $\eta(r)$ with increasing radius.

In models C and D, the clouds are optically thick at the Lyman limit throughout the BLR, and $\eta(r) > 0$ for all lines (Fig. 7). Hence all their responsivity-weighted $\Psi(\tau)$ s are positive. As $\eta(r)$ generally increases outwards in these two models, $R_{RW} > R_{EW}$ for most lines, although they usually agree to within a few light-days.

For the highest ionization lines like $N\ V\ \lambda 1240$ and $He\ II\ \lambda 1640$, $\eta(r) > 0$ at all radii in the models shown here, and hence their responsivity-weighted $\Psi(\tau)$ s are positive. It is, however, physically possible for some HIL species to be depleted as a result of ionization if the ionization parameter is very large. This is most likely for a BLR similar to case II, in which U is large in the inner BLR. Some evidence for this effect is seen for $C\ IV\ \lambda 1549$ at the very inner edge of the BLR in model F. The $He\ II$ lines maintain positive responsivity for larger values of U than do the hydrogen lines, because of the difference in their optical depth structure (Netzer 1991). Sparke (1993) notes that the responsivity of a recombination line may be negative if any increase in the ionization parameter causes a rise in temperature and hence a decrease in the recombination coefficient. This seems

Table 4. The centroids of the responsivity-weighted response functions – the responsivity-weighted radii (R_{RW}) (light-day).

	Model				
	B	C	D	E	F
Ba Cont	13.0	11.6	7.3	7.8	5.1
Pa Cont	10.7	9.6	6.6	7.9	5.4
O VI λ 1035	21.5	2.4	0.9	0.8	0.8
Ly α λ 1215	21.6	24.7	19.9	14.1	9.7
O V λ 1218	26.5	10.8	3.0	1.6	1.1
N V λ 1240	21.6	7.7	2.8	2.1	2.1
Si IV λ 1397	22.4	20.0	14.4	9.9	6.8
O IV] λ 1402	26.3	18.2	9.7	4.5	2.6
C IV λ 1549	26.1	20.7	13.6	8.3	5.5
He II λ 1640	24.7	18.7	12.5	7.1	3.8
Si III] λ 1893	20.3	24.1	21.2	20.6	17.0
C III] λ 1909	25.9	30.1	23.9	16.1	8.8
Mg II λ 2798	46.2	27.7	27.6	28.3	26.9
[O III] λ 4363	31.9	35.6	24.4	11.5	3.5
He II λ 4686	23.4	17.3	11.3	6.4	3.4
H β λ 4861	23.1	19.6	16.4	13.4	10.4
He I λ 5876	14.9	15.2	10.6	11.1	8.5
H α λ 6563	22.1	26.3	23.1	19.9	16.5
P α λ 18751	23.7	28.7	26.3	23.7	21.3

unlikely to be a significant effect for most AGN, because of the relatively small observed range in continuum level variability. The temperatures for the perturbed models calculated here are only a few per cent larger than those for the steady-state models.

Allowing for the drop in R_{RW} for many lines in model B, which could be alleviated by adopting a larger column density normalization, the trends in R_{RW} with s are very similar to those for R_{EW} (Fig. 5). Apart from model B, $R_{RW} > R_{EW}$ for most lines, implying that interpretation of the observed lag using emissivity-weighted $\Psi(\tau)$ s would lead to an overestimate of the BLR size. The form of the emissivity-weighted and responsivity-weighted $\Psi(\tau)$ s, and hence their respective centroids, are most similar where $\eta(r)$ shows the smallest radial variation. The He II lines have the smallest range in $\eta(r)$ for the models shown here although, for models C and D in particular, $\eta(r)$ has a range of a factor of 2 or less for a few other lines, such as Ly α and C III] λ 1909 (Fig. 7). In general, however, the assumption of a constant η , which is implicit in the calculation of the emissivity-weighted $\Psi(\tau)$ s, is a poor approximation. This is particularly true for BLRs containing a mixture of optically thick and thin clouds.

4.3 BLR variability diagnostics

In this paper we consider only spherical BLRs. However, the results shown here have implications for any attempt to deduce the BLR properties using response functions recovered from monitoring data. The radial dependence of the responsivity can lead to the response function for one

BLR model resembling that for another. The responsivity-weighted $\Psi(\tau)$ s for several LILs in models E and F are good examples. These $\Psi(\tau)$ s peak away from zero time-delay. For isotropically emitting clouds assumed to have positive responsivity at all radii, this implies a lack of gas close to the line of sight (e.g. an inclined disc), whereas in fact models E and F are spherical. The non-zero time-delay peaks are a result of some of the gas at small radii having negative responsivity for the LILs, rather than an absence of gas on the corresponding constant-time-delay surface. This is an analogous effect to that of anisotropic line emission, which also results in a $\Psi(\tau)$ for a spherical BLR which peaks away from zero (Ferland et al. 1992; O'Brien et al. 1993a, in preparation). However, unlike the form of $\Psi(\tau)$ shown in Fig. 8(d), anisotropic emission in a spherical BLR would not result in a flat $\Psi(\tau)$ for $0 \leq \tau \leq 2(R_{in}/c)$. Overall, if a recovered response function peaks away from zero time-delay, any interpretation in terms of the BLR structure must take into account both the responsivity and the anisotropy of the line. In the case of BLRs with an inner optically thin region, similar to models E and F, interpretation of a decline in the amplitude of $\Psi(\tau)$ at small time-delay as being due to anisotropic line emission would result in an overestimate of the degree of anisotropy if the gas in the inner BLR has negative responsivity for that line. We note that, as for the responsivity, the anisotropy may vary considerably with radius, depending on the local physical conditions (Goad & O'Brien 1993).

The trends in both the emissivity-weighted and responsivity-weighted $\Psi(\tau)$ s with s suggest that we should use different lines to recover R_{in} and R_{out} . For low-luminosity AGN, R_{in} is probably small, perhaps only a few light-days (Peterson 1988). Thus, to determine R_{in} accurately from monitoring data, a high sampling rate is required. In addition, to make efficient use of the limited available signal-to-noise ratio, it would be best to monitor lines whose variability amplitude to a given continuum event is largest. These will be the HILs, such as O VI λ 1035, N V λ 1240 and He II λ 1640, which are the lines most strongly weighted to the inner radii (small response function centroid), and which therefore respond most coherently to continuum variations and tend to have the largest $\eta(r)$ s. In contrast, to determine R_{out} it would be best to monitor lines whose $\Psi(\tau)$ s have a large amplitude at large time-delays (large response function centroid). These tend to be the LILs, including Mg II λ 2798, C III] λ 1909, Si III] λ 1893, H α and Pa. Some HILs, which tend to have a small amplitude at large time-delay, would give little information on R_{out} in practice, because of the observational difficulty of determining the total extent of $\Psi(\tau)$ for such lines.

For BLRs with similar geometries and continuum fluctuation power-density spectra, those with greater differentiation in the form of the response function between the HILs and LILs will tend to show larger variations in their respective line ratios. Thus, assuming that the HILs and LILs arise from the same BLR component, their observed relative variability amplitudes provide a diagnostic for comparison of the degree of BLR stratification between different AGN, even if the light curves are quite poorly sampled. In performing such a comparison, allowance must be made for the generally larger $\eta(r)$ for HILs compared to LILs. In addition, any comparison between variability models and monitoring data must allow for any contribution by non-variable line com-

ponents, whether due to the narrow-line region or to BLR components which do not respond to the continuum variations. If η is assumed constant throughout the BLR, it can be estimated from the relative observed line and continuum variability amplitudes, having corrected for the lag, and assuming no blurring of the line response because of time-delay effects across the BLR (Krolik et al. 1991). Alternatively, η can be estimated from the integral of the recovered response function over time-delay and the mean variable line and continuum luminosities.

For several blended lines commonly seen in AGN spectra, the models shown here predict that the response function centroid usually differs between the blend components. This may result in detectable variations in the form (e.g. mean wavelength) of the blend following a continuum event. As the $\Psi(\tau)$ s depend on s , such variations are also potential diagnostics of the degree of stratification of the BLR. For the 1400-Å blend we confirm RNF's results that Si iv $\lambda 1397$ is predicted to be stronger than O iv] $\lambda 1402$ (Table 2), whereas most observations show the lines to be fairly equal in strength (Tytler & Fan 1992). The models predict a larger blend mean wavelength for smaller s . The centroids differ by several days for $s < 1.5$, with O iv] $\lambda 1402$ predicted to vary on shorter time-scales. In general, $\eta(r)$ is also larger for O iv] $\lambda 1402$ than for Si iv $\lambda 1397$. The blend mean wavelength will therefore tend to move redward following a continuum outburst. The predicted Si iii] $\lambda 1893$ line strength is about half that of C iii] $\lambda 1909$, which is probably too large given the observed blend mean wavelength (Wilkes 1984). The models predict a smaller blend mean wavelength for smaller s . Due primarily to the smaller critical density for C iii] $\lambda 1909$, the centroid for C iii] $\lambda 1909$ is larger than that for Si iii] $\lambda 1893$ for $0.65 < s < 2$. Even allowing for the smaller value of $\eta(r)$ for Si iii] $\lambda 1893$ compared to C iii] $\lambda 1909$, for models B and C the difference in the centroids is large enough that the blend will tend to move blueward following a continuum outburst. In contrast, C iii] $\lambda 1909$ will respond on shorter time-scales for models E and F. The O v $\lambda 1218$ line tends to vary on a shorter time-scale than Ly α , and has a larger $\eta(r)$. Hence, if the O v line can be detected, the blend mean wavelength will tend to move redward following a continuum outburst.

4.4 Comparison of models with monitoring data

For velocity laws such as that used here, where the higher velocity gas is closer to the centre, a significant ionization parameter gradient would result in the HILs appearing broader and more variable than the LILs on short time-scales. RNF argue that similarities between line profiles tend to rule out large gradients in ionization parameter, although some line profile comparisons (e.g. Shuder 1982; Wilkes 1984; Stripe 1991) support the idea of higher velocity gas being closer in and having a higher density and/or ionization parameter. Stronger support for gradients in ionization parameter and/or density comes from monitoring data for the best-studied AGN. For example, in both NGC 4151 and NGC 5548 the LILs tend to be narrower than the HILs, and the line variability is related to the linewidth in the sense that the broader lines tend to be more variable (Ulrich et al. 1984; Krolik et al. 1991).

In NGC 5548 the line variability properties correlate strongly with ionization state, in that the HILs vary faster and with greater amplitude than do the LILs (Clavel et al. 1991). This pattern of behaviour implies a significant gradient in ionization parameter, such as that in models D, E or F. The recovered $\Psi(\tau)$ s for the UV LILs and H β have non-zero time-delay peaks in NGC 5548 (Krolik et al. 1991; Horne et al. 1991). Krolik et al. suggest that this difference is a result of the LILs and HILs arising from different BLR components, whereas Ferland et al. (1992) propose that the recovered $\Psi(\tau)$ s for all the lines may be consistent with anisotropic line emission from high column density clouds in a spherical BLR. As discussed in Section 4.3, however, the effects of negative responsivity due to an optically thin region must also be considered. For NGC 5548, the shallow slope of the relation between the Ly α flux and the continuum level (Pogge & Peterson 1992) could be due to the presence of optically thin gas 'diluting' the observed Ly α variability amplitude. An alternative explanation, in terms of a smaller continuum variability amplitude shortward of the Lyman limit compared to that observed at 1300 Å, seems unlikely given the short wavelength gap, and the observed hardening of the UV continuum longward of Ly α with increasing continuum level. Sparke (1993) also finds that gas with negative responsivity is required in the inner BLR of NGC 5548 to explain the shape of the CCF for several lines. These include the C iv $\lambda 1549$ and N v $\lambda 1240$ lines, which implies a very high ionization parameter if these lines have negative responsivity because of depletion of their parent ionic species.

O'Brien & Goad (1993) present a test-case non-linear spherical BLR model for NGC 5548 which contains some optically thin clouds in the inner BLR, similar to model F, and allows for anisotropic line emission. This model fits the observed time-scale of the Ly α and Mg ii $\lambda 2798$ variations significantly better than does a linear isotropic model with the same geometry. The model amplitudes are also a better fit, although not perfect, possibly because the degree of non-linearity of the BLR in NGC 5548 is greater than in model F. With such a model, it may be possible to fit the $\Psi(\tau)$ s recovered by Krolik et al. (1991) and Horne et al. (1991) by accurately modelling the responsivity rather than by invoking very large column densities. Such a comparison of course assumes that the method used to recover response functions allows for the possibility of negative amplitudes. This is not the case for the maximum entropy method, which assumes that the response function is positive at all time-delays. Fourier deconvolution does not make this assumption, but this method is severely limited by data quality. If the actual response function is negative at small time-delays, then forcing of positivity is likely to introduce spurious structure in the recovered response function at larger time-delays.

In NGC 4151, the C iii] $\lambda 1909$ line varies more slowly than either C iv $\lambda 1549$ or Mg ii $\lambda 2798$, both of which have a similar lag (Clavel et al. 1990). One possible explanation is that the ionization parameter gradient is small, as in model B, but the mean gas density is high. Such a model would give a similar lag for lines of very different ionization state, like C iv $\lambda 1549$ and Mg ii $\lambda 2798$, whilst C iii] $\lambda 1909$ would be collisionally suppressed over a large fraction of the BLR (see also Ulrich et al. 1991). The Mg ii $\lambda 2798$ line would be expected to have a smaller variability amplitude than C iv $\lambda 1549$, as observed, as its responsivity is usually smaller.

One test of such a model would be to monitor the Si III $\lambda 1893$ line, which has a higher critical density than C III $\lambda 1909$, using high-quality UV spectra.

In Mrk 590 only the cores of the H α and H β lines seem to vary significantly, which Ferland, Korista & Peterson (1990) proposed may be due to the line wings arising from optically thin clouds. The recovered $\Psi(\tau)$ for H β in Mrk 590 shows a decline at small time-delay (Peterson et al. 1992). To test whether this is due to a lack of gas close to the line of sight or to anisotropic line emission, and to determine whether this BLR contains a mixture of optically thick and thin clouds, simultaneous monitoring of several HILs and LILs is required. Several high-luminosity AGN also show evidence for line-core variability only, but these are often optically violent variables (OVVs) or quasars with a relativistic jet (Pérez, Penston & Moles 1989; O'Brien, Zheng & Wilson 1989; Gondhalekar 1990). The profile variability in these AGN may therefore be linked more to anisotropic continuum emission than to optically thin gas (Pérez et al. 1989; O'Brien & Gondhalekar 1991).

5 CONCLUSIONS

The response functions presented in this paper represent the first attempt to calculate in detail the relative variability characteristics of lines covering a wide variety of ionization states, emitted from a BLR with a realistic cloud distribution. The radial line emissivity distributions for a set of steady-state spherical BLR models were calculated explicitly, using a photoionization code for a cloud population whose properties and covering factor were constrained by a radial pressure law. Assuming isotropic line emission and linear response, two sets of response functions were then calculated. For the first set, a change in the continuum level was assumed to change the emissivity of a given line by the same factor for all clouds, thereby giving emissivity-weighted response functions. For the second set, the steady-state models were perturbed by a known amount in ionization parameter, and the radial responsivity distributions, calculated from the resultant change in line emissivities, were used to weight the contribution of each cloud, thereby giving responsivity-weighted response functions.

We found that allowance for the radial responsivity distribution can alter the form of the response function significantly. In particular, depending on the local physical conditions, some lines can have negative responsivity, which can result in a negative response function at some time-delays. This is particularly true for LILs in a BLR in which some of the clouds are optically thin at the Lyman limit. Even where the response function is positive, however, the possibility of negative responsivity must be taken into account when investigating the structure of the BLR and when attempting to quantify anisotropic line emission. Negative response functions are inconsistent with the assumption of positivity made in the maximum entropy method often used to recover response functions from monitoring data, and hence other recovery methods should be explored.

The detailed form of the response functions was found to depend strongly on the ionization parameter and on density gradients. The HIL response function centroids were a factor of 30 smaller than those for the LILs in the most highly stratified model, and even a relatively small ionization

parameter gradient can cause a factor of 5–10 difference. Determination of the relative variability time-scales for HILs and LILs therefore provides a diagnostic of the BLR stratification. Assuming similar BLR geometries, the HIL-to-LIL line ratios will show larger variability amplitudes for more stratified BLRs. Another potential diagnostic is provided by the blend mean wavelength for several blended lines, which will vary following a continuum event if the response function centroids differ between the blend components. The tendency for HIL emission to be weighted towards the inner BLR makes these lines most suitable for determination of the inner radius, as they will respond most coherently to continuum events. The HILs also tend to have the largest responsivities. The amplitude of the response function at large time-delay for some LILs is relatively large, and is fairly insensitive to the pressure law. Such lines are therefore best suited to determination of the outer radius of the BLR.

Although the results presented in this paper represent a major improvement over previous studies in which the radial line emissivity distribution was arbitrarily parametrized, usually as a power law in radius, the assumptions made here that the line emission is isotropic and that all the lines respond linearly to changes in the continuum level are still fairly simplistic. For clouds which are optically thick to the ionizing continuum, many lines have an appreciable optical depth, resulting in anisotropic line emission which affects both the line profile and the observed time-scale on which the line responds to continuum variations (Ferland et al. 1992; Goad & O'Brien 1993; O'Brien et al. 1993a, in preparation). Depending on the local physical conditions, a line may also respond non-linearly to continuum variations. For example, some clouds may change from being optically thick to being optically thin when the continuum level increases. To allow for non-linear line response in general, where the degree of non-linearity is a function of position in the BLR, and hence the relative contribution of clouds at different positions to the variable line emission is a function of continuum level, the explicit calculation of time-dependent emissivities is required, rather than the use of a time-independent linear response function (O'Brien et al. 1993b, in preparation). Although allowance for non-linear response and anisotropic line emission complicates the analysis of monitoring data, the available data suggest that such effects must be taken into account if we are to deduce the BLR properties reliably.

ACKNOWLEDGMENTS

We thank Gary Ferland for a copy of CLOUDY, and the referee, Keith Horne, whose comments led to substantial changes and improvements in this paper. MRG and PTO'B acknowledge the support of an SERC studentship and the SERC IUE project respectively. The computations were performed using VAX and Decstation computers provided by the SERC Starlink project at UCL.

REFERENCES

- Blandford R., McKee C. F., 1982, ApJ, 255, 419
- Clavel J. et al., 1990, MNRAS, 246, 668
- Clavel J. et al., 1991, ApJ, 366, 64

- Collin-Souffrin S., 1986, *A&A*, 166, 115
 Collin-Souffrin S., 1987, *A&A*, 179, 60
 Davidson K., Netzer H., 1979, *Rev. Mod. Phys.*, 51, 715
 Dumont A. M., Collin-Souffrin S., 1990, *A&A*, 229, 313
 Elitzur M., Ferland G. J., 1986, *ApJ*, 305, 35
 Ferland G. J., 1991, Ohio State University Internal Report, 91-01
 Ferland G. J., Persson S. E., 1989, *ApJ*, 347, 656
 Ferland G. J., Korista K. T., Peterson B. M., 1990, *ApJ*, 363, L21
 Ferland G. J., Peterson B. M., Horne K., Welsh W. F., Nahar S. N., 1992, *ApJ*, 387, 95
 Gaskell C. M., 1982, *ApJ*, 263, 79
 Gaskell C. M., Peterson B. M., 1987, *ApJS*, 65, 1
 Gaskell C. M., Sparke L. S., 1986, *ApJ*, 305, 175
 Goad M., O'Brien P. T., 1991, *Starlink Bulletin* No. 8, p. 21
 Goad M., O'Brien P. T., 1993, in 33rd Herstmonceux Conf., *The Nature of Compact Objects in AGN*. Cambridge Univ. Press, Cambridge, in press
 Gondhalekar P. M., 1990, *MNRAS*, 243, 443
 Grevesse N., Anders E., 1989, in Waddington C. J., ed., *AIP Conf. No. 183, Cosmic Abundances of Matter*. AIP, New York
 Horne K., Welsh W. F., Peterson B. M., 1991, *ApJ*, 367, L5
 Koratkar A. P., Gaskell C. M., 1991, *ApJS*, 75, 719
 Krolik J. H., Horne K., Kallman T. R., Malkan M. A., Edelson R. A., Kriss G. A., 1991, *ApJ*, 371, 541
 Kwan J., Krolik J. H., 1981, *ApJ*, 250, 478
 Mannucci F., Salvati M., Stanga R. M., 1992, *ApJ*, 394, 98
 Maoz D. et al., 1991, *ApJ*, 367, 493
 Mathews W. G., Ferland G. J., 1987, *ApJ*, 323, 456
 Netzer H., 1985, *ApJ*, 289, 451
 Netzer H., 1991, in Courvoisier T. J.-L., Mayor M., eds, *Active Galactic Nuclei*. Springer-Verlag, Heidelberg, p. 57
 O'Brien P. T., Goad M., 1993, in 33rd Herstmonceux Conf., *The Nature of Compact Objects in AGN*. Cambridge Univ. Press, Cambridge, in press
 O'Brien P. T., Gondhalekar P. M., 1991, *MNRAS*, 250, 377
 O'Brien P. T., Zheng W., Wilson R., 1989, *MNRAS*, 240, 471
 Penston M. V., 1991, in Miller H. R., Wiita P. J., eds, *Variability of Active Galactic Nuclei*. Cambridge Univ. Press, Cambridge, p. 343
 Pérez E., Penston M. V., Moles M., 1989, *MNRAS*, 239, 55
 Pérez E., Robinson A. R., de la Fuente L., 1992a, *MNRAS*, 255, 502
 Pérez E., Robinson A. R., de la Fuente L., 1992b, *MNRAS*, 256, 103
 Peterson B. M., 1988, *PASP*, 100, 18
 Peterson B. M., Ali B., Horne K., Bertram R., Lane N. J., Pogge R. W., Wagner R. M., 1993, *ApJ*, 402, 469
 Pogge R. W., Peterson B. M., 1992, *AJ*, 103, 1084
 Rees M. J., 1987, *MNRAS*, 228, 47p
 Rees M. J., Netzer H., Ferland G. J., 1989, *ApJ*, 347, 640 (RNF)
 Robinson A., Pérez E., 1990, *MNRAS*, 244, 138
 Sanders B., Phinney E. S., Neugebauer G., Soifer B. T., Matthews K., 1989, *ApJ*, 347, 29
 Shuder J. M., 1982, *ApJ*, 259, 48
 Smith M. G. et al., 1981, *MNRAS*, 195, 437
 Sparke L. S., 1993, *ApJ*, 404, 570
 Stirpe G. M., 1991, *A&A*, 247, 3
 Tytler D., Fan X.-M., 1992, *ApJS*, 79, 1
 Ulrich M. H. et al., 1984, *MNRAS*, 206, 221
 Ulrich M. H., Boksenberg A., Bromage G. E., Clavel J., Elvius A., Penston M. V., Perda G. C., Snijders M. A. J., 1991, *ApJ*, 382, 483
 Welsh W. F., Horne K., 1991, *ApJ*, 379, 586
 Wilkes B. J., 1984, *MNRAS*, 207, 73